Mechanistic theory of margination and flow-induced segregation in confined multicomponent suspensions: Simple shear and Poiseuille flows*

Rafael G. Henríquez Rivera, Xiao Zhang, and Michael D. Graham

Phys. Rev. Fluids **1**, 060501 — Published 18 October 2016

DOI: 10.1103/PhysRevFluids.1.060501

Mechanistic theory of margination and flow-induced segregation in confined multicomponent suspensions: simple shear and Poiseuille flows

Rafael G. Henríquez Rivera, Xiao Zhang, and Michael D. Graham*

Department of Chemical and Biological Engineering

University of Wisconsin-Madison, Madison, WI 53706-1691

(Dated: August 1, 2016)

Abstract

A mechanistic model, derived from kinetic theory, is developed to describe segregation in confined multicomponent suspensions such as blood. It incorporates the two key phenomena arising in these systems at low Reynolds number: hydrodynamic pair collisions and hydrodynamic migration. Two flow profiles are considered: simple shear flow (plane Couette flow) and plane Poiseuille flow. The theory begins by writing the evolution of the number density of each component in the suspension as a master equation with contributions from migration and collisions. By making judicious approximations for the collisions, this system of integrodifferential equations is reduced to a set of drift-diffusion equations. We focus attention on the case of a binary suspension with a deformable primary component that completely dominates the collision dynamics in the system and a trace component that has no effect on the primary. The model captures the phenomena of depletion layer formation and margination observed in confined multicomponent suspensions of deformable particles. The depletion layer thickness of the primary component is predicted to follow a master curve relating it in a specific way to confinement ratio and volume fraction. Results from various sources (experiments, detailed simulations, master equation solutions) with different parameters (flexibility of different components in the suspension, viscosity ratio, confinement, among others) collapse onto the same curve. For sufficiently dilute suspensions the analytical form predicted by the drift-diffusion theory for this curve is in excellent agreement with results from these other sources with only one adjustable parameter. In a binary suspension, several regimes of segregation arise, depending on the value of a "margination parameter" M. Most importantly, in both Couette and Poiseuille flows there is a critical value of M below which a sharp "drainage transition" occurs: one component is completely depleted from the bulk flow to the vicinity of the walls. Direct simulations also exhibit this transition as the size or flexibility ratio of the components changes. Finally, some prior studies suggest a nonmonotonic dependence of margination propensity on volume fraction. We formulate a hypothesis regarding this observation. Theory predictions support the hypothesis, providing further insights into the mechanisms behind margination and segregation phenomena.

* Corresponding author. E-mail: mdgraham@wisc.edu

I. INTRODUCTION

Flow-induced segregation is ubiquitous in multicomponent suspensions and granular materials, including systems as disparate as hard macroscopic particles in air [1], polydisperse droplet suspensions [2], foams [3], and blood. Of particular interest is blood flow. During blood flow both the white blood cells (WBCs) and platelets segregate near the vessel walls, a phenomenon known as margination, while the red blood cells (RBCs) tend to be depleted in the near-wall region, leading to a nonuniform distribution in flow – as indicated by the Fåhræus, Fåhræus-Lindqvist, plasma-skimming, and Zweifach-Fung effects – and consequently to the formation of a so-called cell-free or depletion layer [4–9]. Margination is physiologically vital; for example, WBCs and platelets are needed near the blood vessel walls to respond to infection and for hemostasis. Engineering the margination process has been proposed for microfluidic cell separations in blood (*e.g.,* [10, 11]) as well as for enhanced drug delivery to the vasculature [12, 13].

Blood is a multiphase and multicomponent suspension that is mainly composed of RBCs or erythrocytes, WBCs or leukocytes, and platelets or thrombocytes suspended in plasma. These three main cellular components of blood are present in vastly different quantities and have different physical properties. In humans, RBCs are the predominant component in blood with a volume percentage of 40 % in females and 45 % in males. RBCs and platelets outnumber WBCs by 500:1 and 12-14:1 [14]. RBCs are 7.9 μm across, are highly flexible, and have a biconcave shape. WBCs are more rigid than RBCs and approximately spherical [15]. The WBCs we consider here have a radius of 1-2 times the radius of a RBC. Platelets are also more rigid than RBCs, have a diameter of 2-3 μm and discoidal shape under normal blood flow conditions. The distinctive physical properties of RBCs, WBCs, and platelets play a critical role in many important phenomena, such as margination and cell-free layer formation.

In vivo and *in vitro* studies have focused on characterizing WBC margination based on its dependency on shear rate, hematocrit (Hct), RBC aggregation, and channel width. Most studies have found that WBC margination is higher at low shear rates, characteristic of flow in venules, than at high shear rates, characteristic of flow in arterioles [6, 16, 17]. In the literature, there is yet to be a clear consensus on the dependency of WBC margination on Hct due to the difficulty of carrying out studies in the same system while systematically varying

one parameter at a time. Goldsmith & Spain [16] found WBC margination to be higher at 20 % than at 40 % Hct in tubes of 100 μm in diameter. However, some studies have found a minimal effect of Hct on WBC margination at Hct $<$ 45 %. Firrell & Lipowsky [6] observed that WBC margination was weakly affected at Hct $<$ 45 %, while it increased at Hct $>$ 45 % in vessels of 20-60 μm in diameter. Abbitt & Nash [18] also found WBC margination to be unaffected at Hct $<$ 50 %, but considered a significantly different geometry than is found physiologically: a rectangular duct with a 300 x 0.3 mm cross-section. RBC aggregation has been observed to enhance WBC margination. Pearson & Lipowsky [17] found that enhancing RBC aggregation, via the addition of Dextran 500 as a proaggregating agent, increases WBC margination at shear rates below 450 s^{-1}. Abbitt & Nash [18] observed a similar result at a shear rate of 70 s^{-1}. Recently, Fay *et al.* [19] found that WBC margination is reduced *ex vivo* by exposure to glucocorticoids (*e.g.*, dexamethasone) or catecholamines (*e.g.*, epinephrine), which softens the WBC cytoskeleton. This result is consistent with simulations of binary suspensions of deformable capsules that show that stiff capsules marginate strongly in a suspension of primarily flexible capsules, with the margination decreasing as stiffness contrast decreases [20–22].

WBC margination has also been investigated in several numerical studies [23–26]. Most numerical studies suggest that WBC margination is efficient at intermediate values of Hct = 0.2-0.45 and at relatively low shear rates, characteristic of flow in venules. Freund [24] found no sensitivity of WBC margination to Hct for intermediate Hct = 0.22-0.45. Fedosov *et al.* [25] found a nonmonotonic dependence of WBC margination on Hct with a maximum at intermediate ranges of Hct = 0.25-0.35. Fedosov & Gompper [26] also found a similar result for with WBC margination having a maximum at Hct = 0.2-0.4. They also found WBC margination to be enhanced by RBC aggregation.

Margination of platelets has also been studied in many *in vivo* [5, 27] and *in vitro* [28–33] experimental studies. Most studies have found that platelet margination increases with increasing hematocrit [28, 30, 32, 33]. Woldhuis *et al.* [27] found higher margination of platelets in arterioles than venules and suggested that these differences in platelet distribution between arterioles and venules are not caused by the presence of WBC margination in venules. Most studies have also found platelet margination to increase with increasing shear rate [27, 28, 30]. However, some studies have found a more complex dependency on shear rate [32]. This trend of increasing platelet margination with increasing shear rate is

the opposite to that of WBCs, suggesting that RBC aggregation is not critical for platelet margination. However, the source of this difference remains unknown.

Platelet margination has also been investigated in computational studies [34–36]. Al-Momani *et al.* [34] found platelet margination to increase with increasing Hct for Hct = 0.05-0.15. They showed platelet margination to be correlated to the difference between RBC and platelet size. Fitzgibbon *et al.* [33] found platelet margination to be higher at Hct = 0.2 than Hct = 0.1. Crowl & Fogelson [35] have found platelet margination to be higher at higher shear rates.

The aforementioned phenomena and results can be qualitatively described by two key mechanisms: shear-induced diffusion and wall-induced migration. Shear-induced diffusion has important consequences such as viscosity changes in sheared suspensions [37], augmentation of heat and mass transfer [38], and redistribution of inhomogeneities that balances migration in blood flows [9].

Mainly, two phenomenological models have been used to explain shear-induced transport in monodisperse suspensions of rigid particles: the diffusive flux model and the suspension balance model. The diffusive flux model was introduced by Leighton & Acrivos [39]. In the diffusive flux model, flow-induced collisions between particles lead them to exhibit random displacements from their otherwise unperturbed trajectories, leading to a diffusive behavior. Phillips *et al.* [40] then refined the diffusive flux model to describe shear-induced diffusion based on irreversible two-particle interactions between rigid spheres (*e.g.*, rigid spheres with surface roughness). By scaling arguments they derived particle flux expressions due to two effects: spatially varying collision frequency and spatially varying viscosity. Recently, Kanehl and Stark [41] extended this model to bidisperse suspensions of rigid particles. They found the large particles to segregate toward the center of the channel in pressure-driven flow (*i.e.*, toward the region of low shear). This result agrees with most studies [8, 42–44] of bidisperse suspensions in non-homogeneous shear flows, such as Poiseuille flow, in which the large particles are found to preferentially segregate in regions of low shear rate.

The second main phenomenological theory used to describe shear-induced transport is the suspension balance model. In this model mass and momentum conservation equations are written for the particulate and fluid phases [45–48]. At steady state, for low Reynolds number, and in the absence of a body force, the ensemble-averaged drag force density on the particle, which is modeled analogously to the drag force density in sedimentation, is balanced

by the ensemble-averaged divergence of the particle stress in the momentum conservation equation. This equation is solved for the mean particle velocity, which can then be used to obtain the mean particle flux relative to the mean suspension flow.

Both the diffusive flux model and the suspension balance model can qualitatively capture key effects observed in experiments such as the nonuniformity in the concentration of particles where the concentration is higher in regions of lower shear. However, the models have limitations. For example, in channel flows the particles reach maximum packing in regions of zero shear rate (where the viscosity diverges and the particle stress diverges in the diffusive flux model and suspension balance model, respectively), leading to displaying a sharp aphysical cusp in these regions [45, 47]. To overcome this limitation, nonlocal corrections to the stress based on the concept of suspension temperature, which represents a particle-phase average of a fluctuational velocity [45], and spatial averaging of the constitutive law of stress over a finite volume [46] have been proposed. In the present work, we show that including second order terms in shear rate that are quadratic in position also removes the above-mentioned aphysical cusp.

In suspensions of deformable particles such as drops and capsules, the particles undergo cross-stream motion due to particle migration away from the walls and interactions with other particles. Since the particles are deformable, they migrate away from the wall with velocity $v_m(y)$ [49, 50]. A deformable particle migrates even at zero Reynolds number in simple shear flow. If the velocity gradient is not constant, as in Poiseuille flow, a deformable particle undergoes migration even in the absence of hydrodynamic wall effects [51].

Hudson [52] developed a model based on a drift-diffusion equation for describing migration and shear-induced diffusion in suspensions of drops. The cross-stream flux in the wall-normal direction (y) is

$$j_y = v_m\phi - D_g\frac{\partial\phi}{\partial y}, \tag{1}$$

where ϕ is volume fraction, $D_g = \dot{\gamma}\phi a^2 f_g$ is the gradient diffusivity, f_g is a constant, and $\dot{\gamma}$ is the local shear rate. Hudson used the expression for v_m provided by Chan & Leal [53] for simple shear flows. The gradient diffusivity D_g was obtained by fits of the model. Note that this model does not capture the migration phenomena that arise when the shear rate is not constant (*e.g.*, in Poiseuille flow). Ramachandran *et al.* [54] presented a suspension balance model for a dilute emulsion. The model does not incorporate wall-induced migration but captures effects of shear gradient on transport. Pranay *et al.* [55] used a similar approach

to that of Hudson [52] for describing wall-induced migration and shear-induced diffusion in suspensions of deformable capsules in simple shear flow. They found that the thickness of the cell-free layer scales as ϕ^{-1}. This dependence has also been obtained in scaling analyses [22, 52, 55, 56] as well as with a closed-form solution to a drift-diffusion model derived from kinetic theory [57].

Drift-diffusion models have been developed for describing margination of platelets. Eckestein & Belgacem [58] presented a phenomenological drift-diffusion model to describe their experiments. Their expression is similar to Eq. 1. In contrast to deformable particles, platelets do not exhibit wall-induced migration. The drift term in this model comes from the collisions of platelets with RBCs. Crowl and Fogelson [35] used a Fokker-Planck approach to model platelet margination. They found margination of platelets but lower than that found in detailed numerical simulations. To overcome this they added a drift of platelets toward the wall similar to that assumed by Eckestein & Belgacem [58]. They suggested that platelets drift toward the wall due to one-sided collisions with RBCs. Other authors have argued that the higher wall normal velocity fluctuations in the core flow region is what drives the platelets toward the wall [36]. Drift-diffusion models in which RBCs have an enhanced (i.e. shear-induced) diffusivity, proposed by Zydney & Colton [38], have also been used to study platelet transport over a thrombus [59, 60].

The evolution of number densities in a suspension can be idealized by a kinetic master equation [61, 62]. Kumar & Graham [21] presented such an equation, which incorporates the effects of wall-induced migration and hydrodynamic pair collisions, for a binary suspension of deformable particles in simple shear flow. They also introduced a hydrodynamic Monte Carlo simulation technique to solve the master equation and find steady state concentration distributions. Zurita-Gotor *et al.* [62] and Narsimhan *et al.* [56] employed similar approaches for single-component suspensions of rigid and deformable particles, respectively.

Using the master equation-hydrodynamic Monte Carlo approach and direct simulations, Kumar *et al.* [20–22] showed that in simple shear flow segregation in binary suspensions of deformable capsules that differ in flexibility is mainly driven by heterogenous pair collisions at low volume fractions, while wall-induced migration and heterogeneous pair collisions have comparable contributions at higher volume fractions. In contrast, for the case in which the capsules differ in size, Kumar *et al.* [22] found that the larger wall-induced migration of the large particles is what mainly drives segregation. By treating the collisions as resulting only

in very small particle displacements, the master equation can be simplified to a nonlocal drift-diffusion equation whose solutions for Couette flow agree quantitatively with those of the full master equation [22, 57]. Henríquez Rivera *et al.* [57] further simplified this model into a set of drift-diffusion equations by also taking the collisions to only occur between very closely approaching particles. In the present work we elaborate on this approach. In simple shear flow this model has closed-form solutions to describe segregation in binary suspensions of deformable particles. These results are further discussed later in the present work. Sinha & Graham [63] used this set of drift-diffusion equations and direct simulations to study segregation under simple shear flow in binary suspensions of capsules that differ in shape: spherical and ellipsoidal (oblate or prolate). They showed that the capsules with lower aspect ratio marginate when the ellipsoidal capsules have the same equatorial radius as the spherical capsules. In addition, they showed that the opposite happens when both the ellipsoidal and spherical capsules have the same volume: the ellipsoidal capsules demarginate.

In general, direct simulations of flowing multicomponent suspensions – models of blood – can capture margination phenomena [20, 22, 24, 25, 35, 36, 64–67], but developing a fundamental understanding of underlying mechanisms and parameter dependence from simulations is difficult. It is thus important to have a simple yet mechanistic mathematical model, ideally one with closed-form solutions that reveal parameter dependence, that can distill out the essential phenomena that drive segregation and capture the key effects and transitions.

In the present work, we present a kinetic master equation for both simple shear flow and Poiseuille flow. The kinetic master equation is then simplified into drift-diffusion models. We focus attention on the case of a primary component such as RBCs and a trace component such as WBCs that does not affect the dynamics of the primary component. Cell-free layer and margination results are presented for the two considered flow profiles. Some of the results for simple shear flow appeared in Henríquez Rivera *et al.* [57] but are included in the present work for completeness. Direct simulations of binary suspensions of deformable particles are also presented to corroborate predictions by the theory. Additionally, a hypothesis for describing the effect of hematocrit on margination in blood flow is presented and supported by results from the theory. The models capture key phenomena observed in confined multicomponent suspensions of deformable particles, such as margination and depletion layer formation, and provide further insights into the mechanisms behind

flow-induced segregation.

II. MODEL DERIVATION

A. General Model

We consider a dilute suspension containing N_s types of deformable particles with total volume fraction ϕ undergoing flow in a slit bounded by no-slip walls at $y = 0$ and $y = 2H$ and unbounded in x and z. Quantities referring to a specific component α in the mixture will have subscript α: for example n_α is the number density of component α. We consider here simple shear (plane Couette) and plane Poiseuille flows in the x direction and, consistent with the diluteness assumption, take the local shear rate $\dot{\gamma}$ to be independent of the local number densities. Number densities n_α are assumed to be independent of x and z. In a dilute suspension of particles, where $\phi \ll 1$, the particle-particle interactions can be treated as a sequence of uncorrelated pair collisions [61, 62, 68]. For the moment, we neglect molecular diffusion of the particles. This issue is further addressed below. Since the particles are deformable, they migrate away from the wall during flow with velocity $v_{\alpha m}(y)$ [49, 50]. Fig. 1(a) shows a schematic of the considered system (for Poiseuille flow): a multicomponent suspension of deformable particles in a slit. The evolution of the particle number density distributions can be idealized by a kinetic master equation that captures the migration and collision effects ([21, 22, 56, 57, 62]). Here we derive such an equation and, by making several approximations, refine it to arrive at simplified drift-diffusion models for simple shear flow [57] and Poiseuille flow.

Our starting point is the conservation equation

$$\frac{\partial n_\alpha(y)}{\partial t} = -\frac{\partial}{\partial y} j_\alpha(y), \tag{2}$$

where t is time, y is position in the wall-normal direction, $n_\alpha(y)$ is the number density of component α, and $j_\alpha(y)$ is the flux of component α. Note that n_α and j_α are also functions of t, but for brevity we do not explicitly indicate this dependence. To obtain $j_\alpha(y)$, we start by finding the collision flux, j_α^c, from a flux balance of particles of component α moving across a plane in the domain due to pair collisions with particles of component β. We then incorporate the wall-induced migration, molecular diffusion, and wall volume exclusion fluxes into the model, as described in detail below.

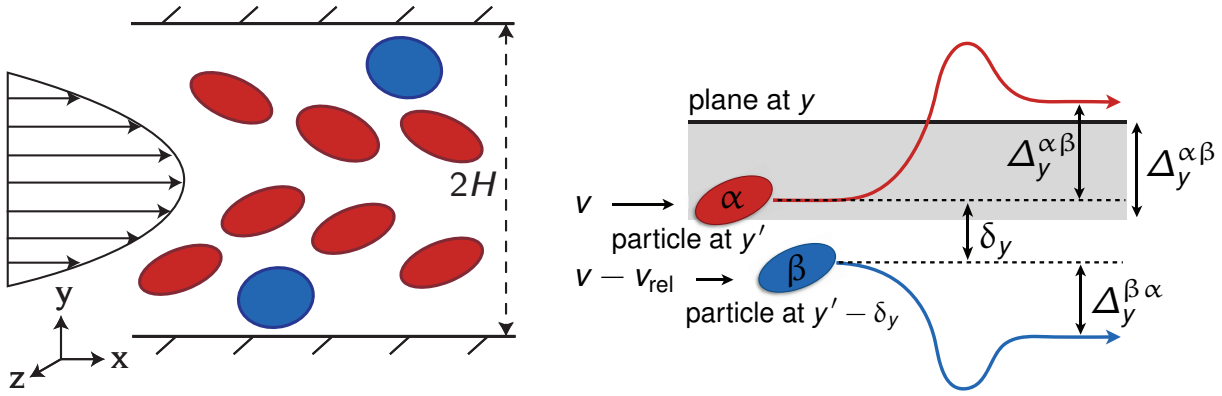

(a) (b)

FIG. 1. (a) Suspension of particles in a slit under plane Poiseuille flow. (b) Pair collision trajectories of particles of species α and β under an imposed flow in the x direction. Far upstream from a pair collision, the particles have a relative velocity $v_{\rm rel}$ between them in the flow (x) direction. Particles of species α get displaced a distance $\Delta_y^{\alpha\beta}$ by collisions with particles of species β. Only the particles of species α that are located within a distance $\Delta_y^{\alpha\beta}$ (illustrated by the shaded area) from the plane located at position y (black solid line) upstream of the collision are pushed across the plane.

For a domain populated by N_s types of deformable particles, we find the flux of α particles being pushed by (pair) collisions with β particles across a plane located at position y. Fig. 1(b) shows a schematic of the x-y plane projection of this type of pair collision in simple shear flow. Far upstream from the pair collision, the particles of components α and β have offsets δ_y and δ_z between them in the y and z directions and are located at y', z' and $y' - \delta_y$, $z' - \delta_z$, respectively. The displacement in the y direction of a particle of component α due to a pair collision with a particle of component β is $\Delta_y^{\alpha\beta}(\delta_y, \delta_z)$. The collision flux at y is given by

$$j_\alpha^c(y) = \sum_{\beta=1}^{N_s} \left\{ \int_{-\infty}^{\infty} \int_{-\infty}^{\infty} \left[\int_{y-\Delta_y^{\alpha\beta}(\delta_y,\delta_z)}^{y} n_\alpha(y') n_\beta(y' - \delta_y) v_{\rm rel}(y', \delta_y) dy' \right] d\delta_y d\delta_z \right\}, \qquad (3)$$

where the sum is over all the types of deformable particles, N_s. The innermost integral corresponds to the particles of component α located at position y', z' that travel across the plane located at y when being displaced a distance $\Delta_y^{\alpha\beta}(\delta_y, \delta_z)$ by collisions with particles of component β located at position $y' - \delta_y, z' - \delta_z$; the x-y plane projection of the described collision is shown in Fig. 1(b). The rate of collisions for a particle of component α is given

by $n_\beta v_{\rm rel}$, where n_β is the number fraction of component β and $v_{\rm rel}$ is the relative velocity between the particles of components α and β as they approach each other for a pair collision. We assume a unidirectional flow in the x direction, so $v_{\rm rel}$ does not depend on z. Equivalent forms of Eq. 3 have been presented in studies of single-component suspensions [56, 61, 62, 68]. By using this form of j_α^c (Eq. 3) in Eq. 2, we have the kinetic master equation, which is a nonlocal integrodifferential model that allows jumps [69].

Since the number densities and $v_{\rm rel}$ do not depend on z, we can perform the outermost integral in Eq. 3 (over δ_z) and obtain

$$\widehat{j_\alpha^c}(y) = \sum_{\beta=1}^{N_s} \left\{ \int_{-\infty}^{\infty} \left[\int_{y-\widehat{\Delta_y^{\alpha\beta}}(\delta_y)}^{y} n_\alpha(y') n_\beta(y'-\delta_y) v_{\rm rel}(y',\delta_y) dy' \right] d\delta_y \right\}, \tag{4}$$

where the symbol '$\widehat{\ }$' over j_α^c and $\Delta_y^{\alpha\beta}$ means that these quantities have been integrated over δ_z. Now dropping the symbol '$\widehat{\ }$' with the understanding that all quantities are now averaged over z, Eq. 4 becomes

$$j_\alpha^c(y) = -\sum_{\beta=1}^{N_s} \int_{-\infty}^{\infty} A d\delta_y, \tag{5}$$

where A is the inner integral in Eq. 4:

$$A = \int_{y-\Delta_y^{\alpha\beta}(\delta_y)}^{y} n_\alpha(y') n_\beta(y'-\delta_y) v_{\rm rel}(y',\delta_y) dy'. \tag{6}$$

Now we make the approximation that $\Delta_y^{\alpha\beta}(\delta_y)$ is only nonzero when δ_y is small, by Taylor expanding A about $\delta_y = 0$:

$$\begin{aligned} A &\approx \int_{y-\Delta_y^{\alpha\beta}(\delta_y)}^{y} n_\alpha(y') \left[n_\beta(y') - \frac{\partial n_\beta(y')}{\partial y'}\delta_y + \frac{1}{2}\frac{\partial^2 n_\beta(y')}{\partial y'^2}\delta_y^2 + \dots \right] \\ &\quad \times \left[\frac{\partial v_{\rm rel}(y')}{\partial y'}\delta_y - \frac{1}{2}\frac{\partial^2 v_{\rm rel}(y')}{\partial y'^2}\delta_y^2 + \dots \right] dy' \\ &= \int_{y-\Delta_y^{\alpha\beta}(\delta_y)}^{y} f_1(y') dy' - \int_{y-\Delta_y^{\alpha\beta}(\delta_y)}^{y} f_2(y') dy' + \int_{y-\Delta_y^{\alpha\beta}(\delta_y)}^{y} f_3(y') dy', \end{aligned}$$

where

$$\begin{aligned} f_1(y',\delta_y) &= n_\alpha(y') n_\beta(y') \left[\frac{\partial v_{\rm rel}(y')}{\partial y'}\delta_y - \frac{1}{2}\frac{\partial^2 v_{\rm rel}(y')}{\partial y'^2}\delta_y^2 + \dots \right], \\ f_2(y',\delta_y) &= n_\alpha(y') \frac{\partial n_\beta(y')}{\partial y'}\delta_y \left[\frac{\partial v_{\rm rel}(y')}{\partial y'}\delta_y - \frac{1}{2}\frac{\partial^2 v_{\rm rel}(y')}{\partial y'^2}\delta_y^2 + \dots \right], \\ f_3(y',\delta_y) &= \frac{1}{2} n_\alpha(y') \frac{\partial^2 n_\beta(y')}{\partial y'^2}\delta_y^2 \left[\frac{\partial v_{\rm rel}(y')}{\partial y'}\delta_y - \frac{1}{2}\frac{\partial^2 v_{\rm rel}(y')}{\partial y'^2}\delta_y^2 + \dots \right]. \end{aligned}$$

We rewrite A as

$$A = \Big[F_1(y,\delta_y) - F_1(y-\Delta_y^{\alpha\beta}(\delta_y),\delta_y)\Big] - \Big[F_2(y,\delta_y) - F_2(y-\Delta_y^{\alpha\beta}(\delta_y),\delta_y)\Big] + \Big[F_3(y,\delta_y) - F_3(y-\Delta_y^{\alpha\beta}(\delta_y),\delta_y)\Big]. \tag{7}$$

Here $F_i(y,\delta_y)$ and $F_i(y-\Delta_y^{\alpha\beta}(\delta_y),\delta_y)$ are the antiderivative of $f_i(y',\delta_y)$ evaluated at $y'=y$ and $y'=y-\Delta_y^{\alpha\beta}(\delta_y)$, where $i=1,2,3$:

$$\int_{y-\Delta_y^{\alpha\beta}(\delta_y)}^{y} f_i(y')dy' = F_i(y,\delta_y) - F_i(y-\Delta_y^{\alpha\beta}(\delta_y),\delta_y). \tag{8}$$

Now we make the additional approximation that $\Delta_y^{\alpha\beta}$ is small, meaning that post-collisional displacements are small. We implement this approximation by carrying out a Taylor expansion of A about $\Delta_y^{\alpha\beta}=0$:

$$\begin{aligned} A \approx & \left[F_1(y,\delta_y) - \left(F_1(y,\delta_y) - \frac{\partial F_1(y,\delta_y)}{\partial y}\Delta_y^{\alpha\beta}(\delta_y) + \frac{1}{2}\frac{\partial^2 F_1(y,\delta_y)}{\partial y^2}(\Delta_y^{\alpha\beta}(\delta_y))^2 + \dots\right)\right] \\ & - \left[F_2(y,\delta_y) - \left(F_2(y,\delta_y) - \frac{\partial F_2(y,\delta_y)}{\partial y}\Delta_y^{\alpha\beta}(\delta_y) + \frac{1}{2}\frac{\partial^2 F_2(y,\delta_y)}{\partial y^2}(\Delta_y^{\alpha\beta}(\delta_y))^2 + \dots\right)\right] \\ & + \left[F_3(y,\delta_y) - \left(F_3(y,\delta_y) - \frac{\partial F_3(y,\delta_y)}{\partial y}\Delta_y^{\alpha\beta}(\delta_y) + \frac{1}{2}\frac{\partial^2 F_3(y,\delta_y)}{\partial y^2}(\Delta_y^{\alpha\beta}(\delta_y))^2 + \dots\right)\right]. \end{aligned} \tag{9}$$

It is necessary to include the terms of $O(\delta_y^2)$, $O((\Delta_y^{\alpha\beta})^2)$, and $O(\delta_y\Delta_y^{\alpha\beta})$ to capture the effect of the nonuniformities in $v_{\rm rel}$ that arise in the Poiseuille flow case. Keeping up to these terms, the collision flux becomes

$$\begin{aligned} j_\alpha^c(y) = -\sum_{\beta=1}^{N_s}\Bigg\{ & \left[n_\alpha(y)n_\beta(y)2\int_0^\infty v_{\rm rel,o}\Delta_y^{\alpha\beta}(\delta_y)d\delta_y\right] \\ & + \left[-n_\alpha(y)\frac{\partial n_\beta(y)}{\partial y}2\int_0^\infty v_{\rm rel,e}\delta_y\Delta_y^{\alpha\beta}(\delta_y)d\delta_y\right] \\ & + \left[-\frac{\partial}{\partial y}\Big(n_\alpha(y)n_\beta(y)\Big)\int_0^\infty v_{\rm rel,e}(\Delta_y^{\alpha\beta}(\delta_y))^2 d\delta_y\right] \\ & + \left[-n_\alpha(y)n_\beta(y)\int_0^\infty \frac{\partial v_{\rm rel,e}}{\partial y}(\Delta_y^{\alpha\beta}(\delta_y))^2 d\delta_y\right]\Bigg\}, \end{aligned} \tag{10}$$

where we have rewritten the relative velocity $v_{\rm rel}(y)$ in terms of its odd and even parts: $v_{\rm rel,o}+v_{\rm rel,e}$. This decomposition aids in simplifying the derivation since integrals from $-\infty$ to ∞ of odd integrands are zero. More details are presented when we discuss specific flows.

The third term in this expression is classical shear-induced diffusion. The second is drift due to "one-sided collisions": *i.e.* due to a higher collision frequency on one side of a particle

of species α than the other due to a gradient in the number density of species β. The first and last are drift terms due to nonuniformities in the relative velocity that arise in the Poiseuille flow case. For single-component suspensions, terms with the same number-density dependence have been proposed on phenomenological grounds (*e.g.*, [40, 45–47]). Note that here however, the multicomponent case is considered and explicit forms for the coefficients in terms of the collisional displacements $\Delta_y^{\alpha\beta}$ are given.

The second key mechanism in the systems under consideration at low Reynolds number is wall-induced migration. We can incorporate wall-induced migration into the model by adding the migration flux

$$j_\alpha^m(y) = v_{\alpha m}(y) n_\alpha(y), \tag{11}$$

where $v_{\alpha m}(y)$ is the wall-normal migration velocity of component α. As an approximation in the dilute limit, we describe the wall-induced hydrodynamic migration velocity of all particles of component α as that of a single particle of component α in a slit. To leading order, a deformable particle in flow near a wall can be described by a point dipole [49, 50]. We superpose the point-force-dipole approximations corresponding to each of the two walls [55]:

$$v_{\alpha m}(y) = K_{\alpha m}\left(\frac{1}{y^2} - \frac{1}{(2H-y)^2}\right). \tag{12}$$

This is a valid approximation for $y/a_\alpha \gg 1$, where a_α is the particle radius of species α; however, it has been shown to be a good approximation for $y/a_\alpha \gtrsim 2$ [55]. The parameter $K_{\alpha m}$ depends linearly on the yy-component of the stresslet generated by the deformable particle [49, 50]. This in turn scales as $\dot{\gamma} g(\mathrm{Ca}_\alpha)$, where $g(\mathrm{Ca}_\alpha)$ is a function that depends on the capillary number Ca_α of component α. The capillary number is a nondimensional group that characterizes particle deformability; for fluid-filled elastic capsules, a common model for cells, it is given by $\mathrm{Ca}_\alpha = \mu\dot{\gamma} a_\alpha / G_\alpha$, where μ is the fluid viscosity and G_α is the membrane shear modulus of component α. Additionally, $K_{\alpha m}$ scales as a_α^4 and also as $\dot{\gamma}^2$ (or as $\dot{\gamma}\mathrm{Ca}_\alpha$) at low $\dot{\gamma}$ with this dependency becoming weaker as $\dot{\gamma}$ increases [22, 55, 70]. We further discuss migration below in the contexts of Couette and Poiseuille flow and conclude by noting that at finite concentration the particle-boundary hydrodynamic interaction that drives migration will be modified by the presence of other particles.

We can also incorporate molecular diffusion by adding the molecular diffusion flux

$$j_\alpha^d(y) = -D_\alpha \frac{\partial n_\alpha(y)}{\partial y}, \tag{13}$$

where D_α is the Brownian diffusivity of component α. We discuss later the significance of this term for describing transport in blood flow.

To account for the fact that particle centers cannot come too close to the wall, we can also include a repulsive excluded volume force. We choose a simple model in which the force starts from zero at $y = a_\alpha$ and increases quadratically as y decreases toward the wall. This force is then

$$F_{\alpha e}(y) = \begin{cases} K_{\alpha e}(y - a_\alpha)^2, & y < a_\alpha \\ 0, & y > a_\alpha, \end{cases} \tag{14}$$

where $K_{\alpha e}$ is a constant and a_α is the particle radius of component α. We take the drift velocity of the particle associated with this force to be (by Stokes' law)

$$v_{\alpha e} = \frac{1}{\zeta_\alpha} F_{\alpha e}(y), \tag{15}$$

where ζ_α is the Stokes friction coefficient for component α. By multiplying this velocity by the number density of component α, we obtain the wall excluded volume flux

$$j_\alpha^e(y) = \frac{1}{\zeta_\alpha} F_{\alpha e}(y) n_\alpha(y). \tag{16}$$

Finally, the total flux of component α is given by combining the fluxes $j_\alpha^m(y)$, $j_\alpha^c(y)$, $j_\alpha^d(y)$, and $j_\alpha^e(y)$:

$$j_\alpha(y) = j_\alpha^m(y) + j_\alpha^c(y) + j_\alpha^d(y) + j_\alpha^e(y). \tag{17}$$

By putting the combined fluxes into Eq. 2, we arrive at a system of coupled drift-diffusion equations for the number densities n_α:

$$\begin{aligned} \frac{\partial n_\alpha(y)}{\partial t} = -\frac{\partial}{\partial y}\Bigg\{ & v_{\alpha m}(y) n_\alpha(y) + \sum_{\beta=1}^{N_s} \Bigg\{ \left[n_\alpha(y) n_\beta(y) 2 \int_0^\infty v_{\mathrm{rel,o}} \Delta_y^{\alpha\beta} d\delta_y \right] \\ & + \left[- n_\alpha(y) \frac{\partial n_\beta(y)}{\partial y} 2 \int_0^\infty v_{\mathrm{rel,e}} \delta_y \Delta_y^{\alpha\beta} d\delta_y \right] + \left[- \frac{\partial}{\partial y}\Big(n_\alpha(y) n_\beta(y) \Big) \int_0^\infty v_{\mathrm{rel,e}} (\Delta_y^{\alpha\beta})^2 d\delta_y \right] \\ & + \left[- n_\alpha(y) n_\beta(y) \int_0^\infty \frac{\partial v_{\mathrm{rel,e}}}{\partial y} (\Delta_y^{\alpha\beta})^2 d\delta_y \right] \Bigg\} - D_\alpha \frac{\partial n_\alpha(y)}{\partial y} + \frac{1}{\zeta_\alpha} F_{\alpha e}(y) n_\alpha(y) \Bigg\}. \end{aligned} \tag{18}$$

Appropriate boundary conditions are no-flux conditions at the walls $y = 0$ and $y = 2H$. In Sec. III, we present results in which symmetry across the centerline $y = H$ is assumed, but this condition is not a requirement of the model. In general, the initial condition can consist of any number density profile that is integrable and nonnegative for all positions. The mean number density of the concentration profile is defined as $\bar{n}_\alpha = \frac{1}{H} \int_0^H n_\alpha(y) dy$.

Analogously, the mean volume fraction of component α is defined as $\bar{\phi}_\alpha = \frac{1}{H}\int_0^H \phi_\alpha(y)dy$, where $\phi_\alpha(y)$ is the volume fraction of component α.

B. Simple Shear Flow

In this section we consider simple shear flow (plane Couette flow with constant shear rate $\dot{\gamma}$). For this case the relative velocity between two particles that are approaching each other for a pair collision is

$$v_{\mathrm{rel}}(y, \delta_y) = \dot{\gamma}\big|\delta_y\big|, \tag{19}$$

and thus

$$v_{\mathrm{rel,e}} = \dot{\gamma}\big|\delta_y\big|, \tag{20}$$

$$v_{\mathrm{rel,o}} = 0, \tag{21}$$

$$\frac{\partial v_{\mathrm{rel,e}}}{\partial y} = 0, \tag{22}$$

$$\frac{\partial v_{\mathrm{rel,o}}}{\partial y} = 0. \tag{23}$$

By substituting Eqs. 20-23 into Eq. 10, the collision flux becomes

$$j_\alpha^c(y) = \sum_{\beta=1}^{N_s}\Bigg[- K_{\alpha\beta c} n_\alpha(y)\frac{\partial\big(n_\beta(y)\dot{\gamma}\big)}{\partial y} - K_{\alpha\beta d}\dot{\gamma}\frac{\partial}{\partial y}\bigg(n_\alpha(y)n_\beta(y)\bigg)\Bigg], \tag{24}$$

where

$$K_{\alpha\beta c} = 2\int_0^{r_{\mathrm{cut}}} \Delta_y^{\alpha\beta}(\delta_y)\delta_y|\delta_y|\, d\delta_y, \tag{25}$$

$$K_{\alpha\beta d} = \int_0^{r_{\mathrm{cut}}} (\Delta_y^{\alpha\beta}(\delta_y))^2|\delta_y|\, d\delta_y. \tag{26}$$

The first and second terms inside the sum represent the collisional drift and shear-induced diffusivity, respectively. Here we assigned a cutoff radius r_{cut} beyond which particle-particle interaction is assumed to be negligible. The parameters $K_{\alpha\beta c}$ and $K_{\alpha\beta d}$ are assumed to be independent of y. In simple shear where $\dot{\gamma}$ is constant this will be a good approximation except perhaps when both particles are within a particle diameter or so from the wall, where the wall will affect the collision dynamics [56]. We remind the reader that the model was integrated over δ_z (see Eq. 4) and therefore $\Delta_y^{\alpha p}(\delta_y)$ has dimensions of length squared. The

convergence of these integrals deserves mention. In the far field each particle appears as a force dipole, so in an unbounded domain the collisional displacements $\Delta_y^{\alpha\beta}$ would decay as δ_y^{-2}. Thus convergence of Eq. 26 is unproblematic irrespective of r_{cut}. For convergence of Eq. 25, r_{cut} must be bounded. An explicit bound is the slit width $2H$. Furthermore, at any finite concentration the spacing between particles scales as $n^{-1/3}$ where n is the total number density. A given particle will effectively only collide with other particles within this range, while particles outside this range would be more strongly affected by their nearer neighbors.

We focus now on the important special case of a binary suspension ($N_s = 2$) composed of a "primary" component ('p') and a "trace" component ('t') such that $n_p \gg n_t$. In this case, only $\beta =$ 'p' in Eq. 24 contributes to the collision fluxes of both the primary and trace components. For simplicity we use the subscripts 'p' and α, where α is 'p' or 't'. The collision flux for such a system is

$$j_\alpha^c(y) = -K_{\alpha pc} n_\alpha(y) \frac{\partial\big(n_p(y)\dot{\gamma}\big)}{\partial y} - K_{\alpha pd}\dot{\gamma}\frac{\partial}{\partial y}\bigg(n_\alpha(y) n_p(y)\bigg). \tag{27}$$

To describe wall-induced hydrodynamic migration, we employ the approach discussed in Sec. II A (Eq. 12) with the parameter $K_{\alpha m}$ being a constant.

With these further idealizations, Eq. 18 reduces to a pair of partial differential equations, which we present here in nondimensional form

$$\begin{aligned}\frac{\partial \phi_\alpha(y)}{\partial t} = -\frac{\partial}{\partial y}\Bigg[&\kappa_{\alpha m}\bigg(\frac{1}{y^2} - \frac{1}{(2\mathrm{C}-y)^2}\bigg)\phi_\alpha(y) - \kappa_{\alpha pc}\phi_\alpha(y)\frac{\partial \phi_p(y)}{\partial y} \\ &- \kappa_{\alpha pd}\frac{\partial}{\partial y}\bigg(\phi_\alpha(y)\phi_p(y)\bigg) - \mathcal{D}_\alpha\frac{\partial \phi_\alpha(y)}{\partial y} + \kappa_{\alpha e}\mathcal{F}_{\alpha e}(y)\phi_\alpha(y)\Bigg],\end{aligned} \tag{28}$$

where α is 'p' for one of the two partial differential equations and 't' for the other. This pair of differential equations is the simplified drift-diffusion model for simple shear flow. Here $\phi_\alpha = n_\alpha V_\alpha$ is the volume fraction of component α, where V_α is the volume per particle of component α, $\mathrm{C} = H/a_p$ is the confinement ratio, $\kappa_{\alpha m} = \frac{K_{\alpha m}}{\dot{\gamma} a_p^3}$, $\kappa_{\alpha pc} = \frac{K_{\alpha pc}}{V_p a_p^2}$, $\kappa_{\alpha pd} = \frac{K_{\alpha pd}}{V_p a_p^2}$, $\mathcal{D}_\alpha = \frac{D_\alpha}{\dot{\gamma} a_p^2}$, $\kappa_{pe} = \frac{K_{pe}}{\dot{\gamma}\zeta_p}$, $\kappa_{te} = \frac{K_{te}\mathrm{S}}{\dot{\gamma}\zeta_p}$,

$$\mathcal{F}_{pe}(y) = \begin{cases}(y-1)^2, & y < 1 \\ 0, & y > 1,\end{cases} \tag{29}$$

$$\mathcal{F}_{te}(y) = \begin{cases}(y-\mathrm{S})^2, & y < \mathrm{S} \\ 0, & y > \mathrm{S},\end{cases} \tag{30}$$

and $\mathrm{S} = a_t/a_p$ is the ratio between the particle radius of the trace component, a_t, and the particle radius of the primary component, a_p (*i.e.,* size ratio). Note that $\mathcal{F}_{\alpha e}(y)$ is the nondimensional form of $F_{\alpha e}(y)$ but without the latter's magnitude $K_{\alpha e}$; the parameter $K_{\alpha e}$ has been extracted for consistency with the other terms in Eq. 28. Time t is nondimensionalized with $\dot{\gamma}^{-1}$ and y with a_p. For simplicity we keep the symbols t and y for their nondimensionalized forms. For a single-component suspension of rigid particles ($N_s = 1, K_{\alpha m} = 0$), a model of similar form was proposed by Phillips *et al.* [40] based on phenomenological arguments first proposed by Leighton & Acrivos [39].

C. Poiseuille Flow

In this section, we consider plane Poiseuille flow. Here the shear rate vanishes at the centerline; this is an important difference from simple shear flow and requires careful treatment there. In particular, at the centerline the relative velocity v_{rel} is quadratic in δ_y rather than linear, leading to terms that are absent in the Couette flow case.

In Poiseuille flow the shear rate and relative velocity vary with position:

$$\dot{\gamma}(y) = \dot{\gamma}_w\Big(1 - \frac{y}{H}\Big), \tag{31}$$

$$\frac{d\dot{\gamma}(y)}{dy} = -\frac{\dot{\gamma}_w}{H}, \tag{32}$$

where $\dot{\gamma}_w$ is the wall shear rate, and

$$v_{\mathrm{rel}}(y, \delta_y) = \left|\dot{\gamma}(y)\delta_y - \frac{1}{2}\frac{d\dot{\gamma}}{dy}\delta_y^2\right| \tag{33}$$

$$= \left|\dot{\gamma}(y)\delta_y + \frac{\dot{\gamma}_w}{2H}\delta_y^2\right|. \tag{34}$$

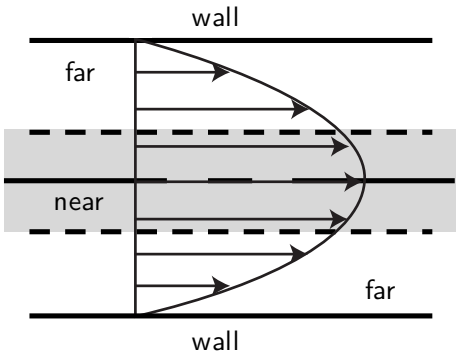

FIG. 2. Schematic of unperturbed plane Poiseuille flow in a slit, highlighting the region near the centerline (shaded area within the dashed lines), where the shear rate is approaching zero. Here "near" and "far" stand for near and far from the centerline, respectively.

Thus

$$v_{\mathrm{rel,e}} = \begin{cases} \dot{\gamma}(y)|\delta_y|, & \text{if } 0 < \delta_y < 2|H-y| \\ \frac{\dot{\gamma}_w}{2H}\delta_y^2, & \text{if } \delta_y > 2|H-y|, \end{cases} \tag{35}$$

$$v_{\mathrm{rel,o}} = \begin{cases} \mathrm{sgn}(H-y)\frac{\dot{\gamma}_w}{2H}\delta_y|\delta_y|, & \text{if } 0 < \delta_y < 2|H-y| \\ \dot{\gamma}(y)|\delta_y|, & \text{if } \delta_y > 2|H-y|, \end{cases} \tag{36}$$

$$\frac{\partial v_{\mathrm{rel,e}}}{\partial y} = \begin{cases} -\frac{\dot{\gamma}_w}{H}|\delta_y|, & \text{if } 0 < \delta_y < 2|H-y| \\ 0, & \text{if } \delta_y > 2|H-y|, \end{cases} \tag{37}$$

$$\frac{\partial v_{\mathrm{rel,o}}}{\partial y} = \begin{cases} 0, & \text{if } 0 < \delta_y < 2|H-y| \\ -\frac{\dot{\gamma}_w}{H}\delta_y, & \text{if } \delta_y > 2|H-y|. \end{cases} \tag{38}$$

We keep the expression $\mathrm{sgn}\,(H-y)$ for now even though our focus here is the bottom half of the domain ($y < H$).

Near the centerline ($y = H$) it is necessary to include the quadratic terms in δ_y of Eqs. 35-38 since, as mentioned above, the shear rate vanishes at the centerline. This region is highlighted (shaded area) in Fig. 2. Fig. 3 shows v_{rel}, $v_{\mathrm{rel,e}}$, and $v_{\mathrm{rel,o}}$ as functions of δ_y for various values of y. In this figure we can clearly observe two distinct regions: (a) away from the centerline where $0 < \delta_y < 2|H-y|$ and (b) near the centerline where $\delta_y > 2|H-y|$. Recall that $v_{\mathrm{rel}} = v_{\mathrm{rel,e}} + v_{\mathrm{rel,o}}$. At the centerline (black dashed line) where the shear rate is zero, $v_{\mathrm{rel,o}}$ is zero and $v_{\mathrm{rel,e}}$ scales quadratically with δ_y; thus v_{rel} also scales quadratically

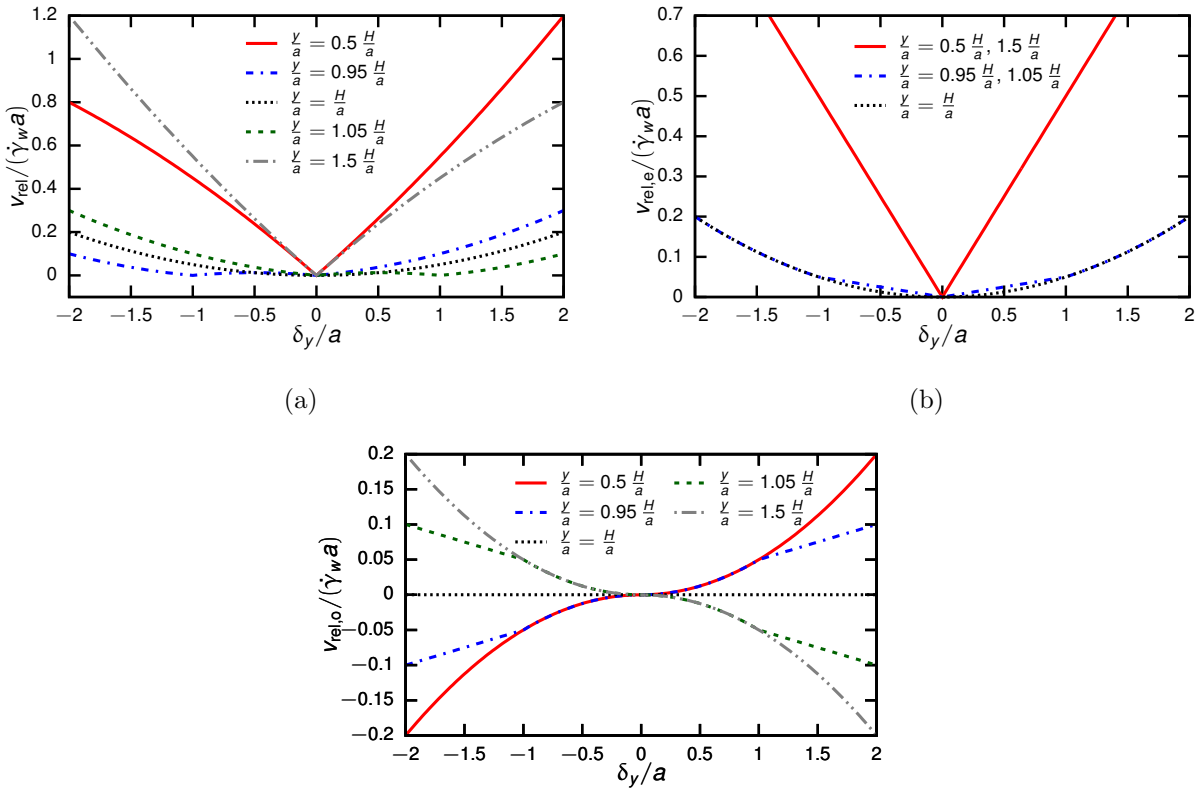

FIG. 3. (a) $\frac{v_{\rm rel}}{\dot\gamma_w a}$, (b) $\frac{v_{\rm rel,e}}{\dot\gamma_w a}$, and (c) $\frac{v_{\rm rel,o}}{\dot\gamma_w a}$ in plane Poiseuille flow as functions of $\frac{\delta_y}{a}$ for different $\frac{y}{a}$ positions, where a is the radius of the particle.

with δ_y (*i.e.*, the term that is quadratic in δ_y is the dominant one at the centerline). As y increases or decreases from $y = H$, moving away from the centerline, the shear rate increases and the term that is linear in δ_y becomes dominant. As above we apply a cutoff radius $r_{\rm cut}$ beyond which particle-particle interaction is negligible. The collision flux in the two regions is:

(a) away from the centerline ($0 < r_{\rm cut} < 2|H - y|$):

$$
\begin{aligned}
j^c_\alpha(y) = \sum_{\beta=1}^{N_s} \Bigg\{ & \left[n_\alpha(y) n_\beta(y) 2 \int_0^{r_{\rm cut}} {\rm sgn}(y<H) \frac{\dot\gamma_w}{2H} \delta_y |\delta_y| \Delta_y^{\alpha\beta} d\delta_y \right] \\
& + \left[- n_\alpha(y) \frac{\partial n_\beta(y)}{\partial y} 2 \int_0^{r_{\rm cut}} \dot\gamma(y) \delta_y |\delta_y| \Delta_y^{\alpha\beta} d\delta_y \right] \\
& + \left[- \frac{\partial}{\partial y} \Big(n_\alpha(y) n_\beta(y) \Big) \int_0^{r_{\rm cut}} \dot\gamma(y) |\delta_y| (\Delta_y^{\alpha\beta})^2 d\delta_y \right] \\
& + \left[n_\alpha(y) n_\beta(y) \int_0^{r_{\rm cut}} \frac{\dot\gamma_w}{H} |\delta_y| (\Delta_y^{\alpha\beta})^2 d\delta_y \right] \Bigg\},
\end{aligned}
\tag{39}
$$

(b) near the centerline ($r_{\rm cut} > 2|H-y|$):

$$
\begin{aligned}
j^c_\alpha(y) = \sum_{\beta=1}^{N_s} \Bigg\{ & \Bigg[- n_\alpha(y) \frac{\partial n_\beta(y)}{\partial y} 2 \int_{2|H-y|}^{r_{\rm cut}} \frac{\dot\gamma_w}{2H} \delta_y^3 \Delta_y^{\alpha\beta} d\delta_y \Bigg] \\
& + \Bigg[- \frac{\partial}{\partial y} \Big(n_\alpha(y) n_\beta(y) \Big) \int_{2|H-y|}^{r_{\rm cut}} \frac{\dot\gamma_w}{2H} \delta_y^2 (\Delta_y^{\alpha\beta})^2 d\delta_y \Bigg] \\
& + \Bigg[n_\alpha(y) n_\beta(y) 2 \int_0^{2|H-y|} {\rm sgn}(y<H) \frac{\dot\gamma_w}{2H} \delta_y |\delta_y| \Delta_y^{\alpha\beta} d\delta_y \Bigg] \\
& + \Bigg[n_\alpha(y) n_\beta(y) \dot\gamma(y) 2 \int_{2|H-y|}^{r_{\rm cut}} \delta_y \Delta_y^{\alpha\beta} d\delta_y \Bigg] \\
& + \Bigg[- n_\alpha(y) \frac{\partial n_\beta(y)}{\partial y} 2 \int_0^{2|H-y|} \dot\gamma(y) \delta_y |\delta_y| \Delta_y^{\alpha\beta} d\delta_y \Bigg] \\
& + \Bigg[- \frac{\partial}{\partial y} \Big(n_\alpha(y) n_\beta(y) \Big) \int_0^{2|H-y|} \dot\gamma(y) |\delta_y| (\Delta_y^{\alpha\beta})^2 d\delta_y \Bigg] \\
& + \Bigg[n_\alpha(y) n_\beta(y) \int_0^{2|H-y|} \frac{\dot\gamma_w}{H} |\delta_y| (\Delta_y^{\alpha\beta})^2 d\delta_y \Bigg] \Bigg\}. \qquad (40)
\end{aligned}
$$

Notice that the last five terms of Eq. 40 vanish at the centerline.

This model is now rather complex and cumbersome. To proceed we will make a further approximation, neglecting the terms in Eq. 40 that vanish on the centerline. Then by combining Eq. 39 and the first two terms of Eq. 40 and by simplifying the result, we obtain

$$
\begin{aligned}
j^c_\alpha(y) = \sum_{\beta=1}^{N_s} \Bigg\{ & - K_{\alpha\beta c} \Bigg[\frac{\partial}{\partial y} \Big(n_\beta(y) \dot\gamma(y) \Big) + h \frac{\dot\gamma_w}{2H} n_\beta(y) \Bigg] n_\alpha(y) \\
& - K_{\alpha\beta d} \frac{\partial}{\partial y} \Big(n_\alpha(y) n_\beta(y) \dot\gamma(y) \Big) \\
& - \frac{1}{2} K'_{\alpha\beta c} n_\alpha(y) \frac{\partial n_\beta(y)}{\partial y} \frac{\dot\gamma_w}{H} - \frac{1}{2} K'_{\alpha\beta d} \frac{\partial}{\partial y} \Big(n_\alpha(y) n_\beta(y) \Big) \frac{\dot\gamma_w}{H} \Bigg\}, \qquad (41)
\end{aligned}
$$

where

$$K_{\alpha\beta c} = 2 \int_0^{r_{\rm cut}} \delta_y |\delta_y| \Delta_y^{\alpha\beta}(\delta_y) d\delta_y, \qquad (42)$$

$$K_{\alpha\beta d} = \int_0^{r_{\rm cut}} |\delta_y| (\Delta_y^{\alpha\beta}(\delta_y))^2 d\delta_y, \qquad (43)$$

$$K'_{\alpha\beta c} = 2 \int_{2|H-y|}^{r_{\rm cut}} \delta_y^3 \Delta_y^{\alpha\beta}(\delta_y) d\delta_y, \qquad (44)$$

$$K'_{\alpha\beta d} = \int_{2|H-y|}^{r_{\rm cut}} \delta_y^2 (\Delta_y^{\alpha\beta}(\delta_y))^2 d\delta_y, \qquad (45)$$

and

$$h = 2 + {\rm sgn}\,(y - H). \qquad (46)$$

The primed parameters $K'_{\alpha\beta c}$ and $K'_{\alpha\beta d}$ are absent in the Couette flow case. All four parameters $K_{\alpha\beta c}$, $K_{\alpha\beta d}$, $K'_{\alpha\beta c}$, and $K'_{\alpha\beta d}$ depend on the collision function $\Delta_y^{\alpha\beta}$, which in turn may depend on position via the local shear rate, because the particle deformations also depend on shear rate. However, prior work on pair collisions of elastic capsules [71] indicates that the collisional displacements are only weakly dependent on Ca except when Ca is very small. Furthermore, as noted above, the wall only plays a role for collisions that occur very close to the wall. Therefore, we take these parameters to be independent of position. Here our focus for the derivation of the model is the bottom half of the domain ($y < H$) – we will assume symmetry across the centerline – so we use $h = 1$ from this point forward.

The first term in Eq. 41 represents the collisional drift: the $-K_{\alpha\beta c}\frac{\partial}{\partial y}\left(n_\beta(y)\dot{\gamma}(y)\right)n_\alpha(y)$ part appears in simple shear flow (Eq. 24) but the $-K_{\alpha\beta c}\frac{\dot{\gamma}_w}{2H}n_\beta(y)n_\alpha(y)$ part does not. The second term is the shear-induced diffusion term. The third and fourth terms are modifications to the collisional drift and shear-induced diffusion near the centerline, respectively; they do not appear in the simple shear flow case. Miller & Morris [47] added a term similar to the one containing $K'_{\alpha\beta d}$ to their model of rigid-sphere suspensions based on the physical argument that shear-induced diffusivity should not be zero at the centerline. Here we see that it arises naturally when the quadratic term in the relative velocity is kept.

As in the simple shear flow case, we consider the case of a binary suspension composed of a "primary" component ('p') and a "trace" ('t') component such that $n_p \gg n_t$. We use the subscripts 'p' and α , where α is 'p' or 't'. The collision flux for this system is

$$\begin{aligned} j_\alpha^c(y) = &-K_{\alpha pc}\left[\frac{\partial}{\partial y}\left(n_p(y)\dot{\gamma}(y)\right) + \frac{\dot{\gamma}_w}{2H}n_p(y)\right]n_\alpha(y) \\ &- K_{\alpha pd}\frac{\partial}{\partial y}\left(n_\alpha(y)n_p(y)\dot{\gamma}(y)\right) \\ &- \frac{1}{2}K'_{\alpha pc}n_\alpha(y)\frac{\partial n_p(y)}{\partial y}\frac{\dot{\gamma}_w}{H} - \frac{1}{2}K'_{\alpha pd}\frac{\partial}{\partial y}\left(n_\alpha(y)n_p(y)\right)\frac{\dot{\gamma}_w}{H}. \end{aligned} \tag{47}$$

To describe the wall-induced hydrodynamic migration velocity, we use Eq. 12 with $K_{\alpha m} = K_{\alpha w}\dot{\gamma}(y)\frac{\mathrm{Ca}_\alpha\left(1-\frac{y}{H}\right)}{\kappa_1+\mathrm{Ca}_\alpha\left(1-\frac{y}{H}\right)}$. Here $K_{\alpha w}$ is the magnitude of the wall-induced migration velocity of component α and κ_1 is a nondimensional constant; they are both fitting parameters obtained from boundary integral simulations of a single capsule migrating away from the closest wall under plane Poiseuille flow in a slit for different values of Ca_α (*cf.* [20, 22, 72]). The above expression for $K_{\alpha m}$ follows the scaling, mentioned earlier, of $K_{\alpha m}$ as $\dot{\gamma}\mathrm{Ca}_\alpha$ at low Ca_α with this dependency becoming weaker as Ca_α increases until $K_{\alpha m}$ reaches a plateau. In Poiseuille

flow we base Ca_α on the wall shear rate $\dot{\gamma}_w$: $\mathrm{Ca}_\alpha = \mu\dot{\gamma}_w a_\alpha/G_\alpha$.

If the velocity gradient is not constant as in Poiseuille flow, a deformable particle experiences migration even in the absence of confinement [51]. Chan & Leal [53] found an analytical expression for the migration velocity of a drop in an unbounded plane Poiseuille flow in the limit of small deformation. Helmy & Barthès-Biesel [73] also found an analytical expression for the migration velocity of a capsule in unbounded pipe flow in the limit of $\mathrm{Ca}_\alpha \ll 1$. Their results predict a linear dependence of migration velocity on $\dot{\gamma}_w$, Ca_α, and distance from the center. As in the case of wall-induced migration, we assume saturation of the shear gradient induced migration at high Ca_α. The total migration velocity, including its wall and shear gradient induced migration components, in Poiseuille flow is then

$$v_{\alpha m}(y) = \frac{\dot{\gamma}_w \mathrm{Ca}_\alpha \left(1-\frac{y}{H}\right)}{\kappa_1 + \mathrm{Ca}_\alpha\left(1-\frac{y}{H}\right)}\left[K_{\alpha w}\left(1-\frac{y}{H}\right)\left(\frac{1}{y^2}-\frac{1}{(2H-y)^2}\right)+K_{\alpha g}\right]. \tag{48}$$

The parameter $K_{\alpha g}$ is the magnitude of the shear gradient induced migration and is obtained from the same boundary integral simulations used for finding $K_{\alpha w}$ and κ_1.

Finally, for Poiseuille flow Eq. 18 reduces to a pair of partial differential equations, which we present here in nondimensional form

$$\begin{aligned}\frac{\partial \phi_\alpha(y)}{\partial t} = -\frac{\partial}{\partial y}\Bigg\{ &\frac{\mathrm{Ca}_\alpha(1-\frac{y}{\mathrm{C}})}{\kappa_1+\mathrm{Ca}_\alpha(1-\frac{y}{\mathrm{C}})}\Bigg[\kappa_{\alpha w}\Big(1-\frac{y}{\mathrm{C}}\Big)\Big(\frac{1}{y^2}-\frac{1}{(2\mathrm{C}-y)^2}\Big)\\ &+\kappa_{\alpha g}\Bigg]\phi_\alpha(y) - \kappa_{\alpha\beta c}\Bigg[\frac{\partial}{\partial y}\Big(\phi_p(y)\big(1-\frac{y}{\mathrm{C}}\big)\Big)+\frac{1}{2\mathrm{C}}\phi_p(y)\Bigg]\phi_\alpha(y)\\ &-\kappa_{\alpha\beta d}\frac{\partial}{\partial y}\Big(\phi_\alpha(y)\phi_p(y)\Big(1-\frac{y}{\mathrm{C}}\Big)\Big) - \kappa'_{\alpha\beta c}\frac{1}{2\mathrm{C}}\phi_\alpha(y)\frac{\partial\phi_p(y)}{\partial y}\\ &-\kappa'_{\alpha\beta d}\frac{1}{2\mathrm{C}}\frac{\partial}{\partial y}\Big(\phi_\alpha(y)\phi_p(y)\Big) - \mathcal{D}_\alpha\frac{\partial\phi_\alpha(y)}{\partial y}+\kappa_{\alpha e}\mathcal{F}_{\alpha e}(y)\phi_\alpha(y)\Bigg\}.\end{aligned} \tag{49}$$

Here $\kappa_{\alpha w} = \frac{K_{\alpha w}}{a_p^3}$, $\kappa_{\alpha g} = \frac{K_{\alpha g}}{a_p}$, $\kappa'_{\alpha pc} = \frac{K'_{\alpha pc}}{V_p a_p^3}$, $\kappa'_{\alpha pd} = \frac{K'_{\alpha pd}}{V_p a_p^3}$, $\mathcal{D}_\alpha = \frac{D_\alpha}{\dot{\gamma}_w a_p^2}$, $\kappa_{pe} = \frac{K_{pe}}{\dot{\gamma}_w \zeta_p}$, and $\kappa_{te} = \frac{K_{te}\mathrm{S}}{\dot{\gamma}_w\zeta_p}$; the rest of the symbols in Eq. 49 are defined as in Sec. II B.

III. RESULTS

A. Simple Shear Flow

In this section we present results of the drift-diffusion model for simple shear flow (Eq. 28). Some of these are presented in [57] and are repeated here for completeness. Unless otherwise

noted, in this section we neglect molecular diffusion and the wall excluded volume effect: the former effect is negligible for sufficiently large particles as discussed below and the latter is negligible except at high volume fraction, a case we address in Section III C. An important feature of the pair of differential equations represented by Eq. 28 in the absence of these effects is that steady state solutions with no-flux boundary conditions at the wall ($y = 0$) and centerline ($y = \mathrm{C}$) can be found analytically. For a given mean volume fraction $\bar{\phi}_p$, we find that the volume fraction $\phi_p(y)$ of the primary component satisfies

$$\phi_p = \begin{cases} 0, & y < l_d \\ \frac{2\mathrm{C}^2\bar{\phi}_p}{2\mathrm{C}(\mathrm{C}-l_d)-l_d(2\mathrm{C}-l_d)\ln\left(\frac{2\mathrm{C}-l_d}{l_d}\right)}\left(1-\frac{l_d}{y}\frac{(2\mathrm{C}-l_d)}{(2\mathrm{C}-y)}\right), & y > l_d \end{cases}, \tag{50}$$

where $\eta_p = \frac{\kappa_{pm}}{\kappa_{ppc}+2\kappa_{ppd}}$, and l_d is the nondimensional cell-free or depletion layer thickness. An implicit relation between l_d and $\bar{\phi}_p$ is given by

$$\bar{\phi}_p = \eta_p\left(\frac{2(\mathrm{C}-l_d)}{l_d(2\mathrm{C}-l_d)} - \frac{1}{\mathrm{C}}\ln\left(\frac{2\mathrm{C}-l_d}{l_d}\right)\right), \tag{51}$$

This will remain valid even in the presence of the wall-exclusion effect as long as l_d is greater than the radius of the primary component. Note the simple linear dependence on η_p: as long as $0 < l_d < \mathrm{C}$, the only role of the collision and migration parameters is to scale the mean volume fraction. It is illuminating to rearrange this expression to yield

$$\frac{\bar{\phi}_p\mathrm{C}}{\eta_p} = 2\frac{\mathrm{C}}{l_d}\frac{(1-\frac{l_d}{\mathrm{C}})}{(2-\frac{l_d}{\mathrm{C}})} - \ln\left(2\frac{\mathrm{C}}{l_d}-1\right). \tag{52}$$

Observe that this result implies that $\bar{\phi}_p\mathrm{C}/\eta_p$ is a function of l_d/C (or vice versa), so given the single adjustable parameter η_p, all results should fall onto a master curve when plotted in terms of these two quantities.

To assess this prediction, we fit η_p to results from several sources. First we consider simple shear flow results from numerical simulations of pure suspensions of deformable capsules with $\mathrm{Ca} = 0.2$ and 0.5 for $\mathrm{C} = 5.08$ [22], as shown in 4(a), and from a nonlocal (master equation) model for RBCs with $\mathrm{Ca} = 1$ for $\mathrm{C} = 7$ [56], as shown in Fig. 4(b). We also fit *pressure-driven* flow results from *in vitro* experiments with blood in small glass capillaries where the confinement ratio (in this case tube radius over RBC radius) is 7.15 [74] as shown in Fig. 4(c). The (tube) hematocrit Hct (*i.e.*, $\bar{\phi}_p$) in Fig. 4(c) is calculated from feed hematocrit $\mathrm{Hct_F}$ using a correlation from Pries *et al.* [75] that captures the Fåhræus effect – the reduction of

(tube) hematocrit relative to feed hematocrit – for human and rat blood:

$$\frac{\mathrm{Hct}}{\mathrm{Hct_F}} = \mathrm{Hct_F}(1-\mathrm{Hct_F})(1+1.7\,\mathrm{e}^{-0.415D}-0.6\,\mathrm{e}^{-0.011D}), \tag{53}$$

where D is the vessel diameter in μm.

The only fitting parameter in Figs. 4(a)-4(c) is η_p; its value for the three cases is reported in the figures. The reported η_p were obtained from fitting the data for $\bar{\phi}_p \lesssim 0.2$ (our theory only incorporates pair interactions and thus cannot be expected to give quantitative agreement at high $\bar{\phi}_p$). In all three figures, l_d decreases with increasing $\bar{\phi}_p$. The fits using Eq. 51 agree very well with the results at $\bar{\phi}_p \lesssim 0.2$, which is consistent with the diluteness assumption in the formulation of the model.

Additionally, we fit results from *in vivo* observations of l_d in arterioles of various radii in the rat cremaster muscle at normal arterial pressure and hematocrit (*i.e.*, $\bar{\phi}_p$) of $0.31 < \mathrm{Hct} < 0.39$ [76], which is also calculated using Eq. 53. These results as well as the results in Figs. 4(a)-4(c) are shown in Fig. 4(d), in terms of the quantities l_d/C and $\bar{\phi}_p\mathrm{C}/\eta_p$. The values of η_p are shown in the figure caption and are all in the range $0.36 < \eta_p < 0.85$. Remarkably, nearly all the data points collapse onto a single master curve, even results for $\bar{\phi}_p$ beyond the range considered for the fittings shown in Figs. 4(a)-4(c), and even for results in pressure-driven flow. The only data points that significantly deviate are the *in vivo* measurements for arterioles with radius less than 10 μm (a rat RBC has radius of about 3 μm). This means that independent of the form of our theory, the relationship between $\bar{\phi}_p$ and l_d is set by only one adjustable parameter (η_p). Our specific results slightly overpredicts l_d/C at high $\bar{\phi}_p\mathrm{C}$.

In addition, $l_d \to \eta_p/\bar{\phi}_p$ in the unconfined limit $\mathrm{C} \to \infty$, confirming the ϕ^{-1} dependence found earlier in scaling analyses [22, 52, 55, 56]. More generally, Eq. 51 analytically captures the dependence of the cell-free layer thickness on the volume fraction, degree of confinement, and particle properties. For completeness we note that an explicit expression for l_d can be formulated in terms of the centerline volume fraction of the primary component, ϕ_{pc}, rather than $\bar{\phi}_p$:

$$l_d = \mathrm{C}\left(1-\sqrt{\frac{\mathrm{C}\phi_{pc}}{2\eta_p+\mathrm{C}\phi_{pc}}}\right). \tag{54}$$

As $\mathrm{C} \to \infty$, $\phi_{pc} \to \bar{\phi}_p$.

The concentration profile for the primary component given by the closed-form solution (Eq. 50) is illustrated as the black solid curve in Fig. 5. We plot this in the form $\phi_p/\bar{\phi}_p$

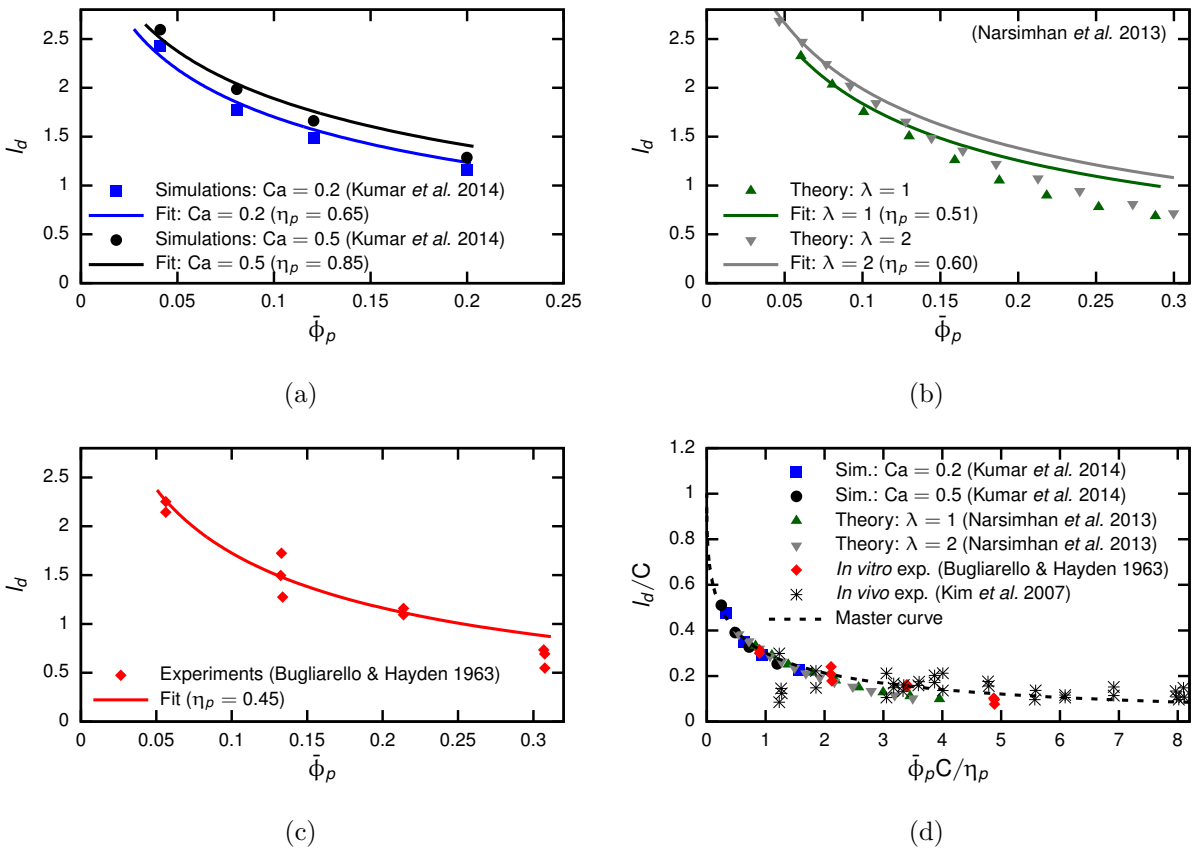

FIG. 4. Plots of cell-free layer thickness l_d (nondimensionalized with particle radius) *vs.* $\bar{\phi}_p$ from various sources, along with fits to Eq. 52. The fitting parameter η_p is reported in the plots. The fits are done to (a) boundary integral simulations of pure suspensions of deformable capsules with Ca = 0.2 and 0.5 for C = 5.08 in simple shear flow [22]; (b) integrodifferential model for red blood cells with Ca = 1 and viscosity ratios, λ, of 1 and 2 for C = 7 in simple shear flow [56]; (c) *in vitro* experiments of blood in small glass capillaries in pressure-driven flow for C = 7.15 [74]. In (c) the capillary number varies from 0.4 to 1.6. In (d) l_d/C is plotted against $\bar{\phi}_p$C/η_p as suggested by the form of Eq. 52. Results from *in vivo* experiments (star symbols) in arterioles in the rat cremaster muscle [76] are also included in (d). For these results $\eta_p = 0.36$ and was obtained by fitting the data corresponding to vessels with diameters of at least three times the RBC diameter in rats; for reference, the results included in the fit correspond to roughly $\bar{\phi}_p$C/$\eta_p > 2.5$ in (d). The black dashed curve in (d) is Eq. 51.

as a function of y. The bottom half of the channel $0 < y <$ C is shown – in this and all future profile plots we assume symmetry across the centerline. The solution is zero within the cell-free layer $y < l_d$ and increases with increasing y, reaching a maximum at

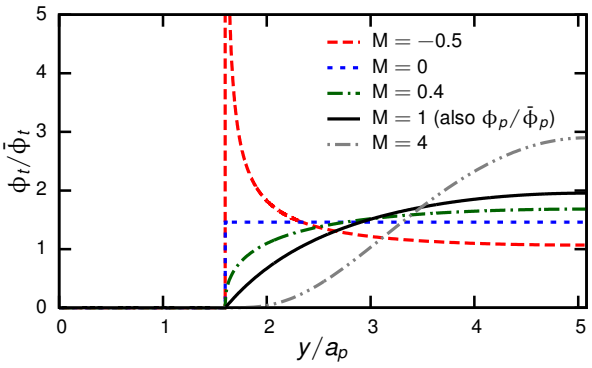

FIG. 5. Steady state volume fraction profiles of $\phi_p/\bar{\phi}_p$ (black solid line) and $\phi_t/\bar{\phi}_t$ for various values of M. (The curves coincide when M = 1.) Here $\bar{\phi}_p = 0.12$, $\phi_{pc} = 0.23$, C = 5.08, $\kappa_{pm} = 0.11$, $\kappa_{ppc} = 0.02$, and $\kappa_{ppd} = 0.07$, resulting in $l_d = 1.6$ (extracted from simulation results in [22]). For simplicity, $\kappa_{tpd} = \kappa_{ppd}$ and $\kappa_{tpc} = \kappa_{ppc}$. We vary M by changing κ_{tm}.

$y = \mathrm{C}$. While this solution captures the presence and parameter dependence of the cell-free layer, detailed simulations [20, 22, 56] reveal a local maximum in ϕ_p near the wall, which the present model does not predict. The full master equation does predict this, as does a nonlocal drift-diffusion approach that assumes that the collision function $\Delta_y^{\alpha\beta}$ is small, but not short-ranged [22, 56].

For the trace component, an analytical steady state solution can also be found: it is

$$\phi_t = \begin{cases} 0, & y < l_d \\ \phi_{tc}\left(\frac{\phi_p(y)}{\phi_{pc}}\right)^{\mathrm{M}}, & y > l_d \end{cases}, \tag{55}$$

where $\phi_p(y)$ is the steady state solution for ϕ_p found above, ϕ_{tc} is the volume fraction of the trace component at the centerline, and

$$\mathrm{M} = \frac{\kappa_{ppc} + 2\kappa_{ppd}}{\kappa_{tpd}}\left(\frac{\kappa_{tm}}{\kappa_{pm}} - \frac{\kappa_{tpc} + \kappa_{tpd}}{\kappa_{ppc} + 2\kappa_{ppd}}\right). \tag{56}$$

Remarkably, this single quantity, which we call the *margination parameter*, determines the qualitative nature of the concentration profile as we now describe.

The sign of M is determined by the competition between the ratio of the migration velocities of the two components, $\frac{\kappa_{tm}}{\kappa_{pm}}$, and the ratio of the collisional terms, $\frac{\kappa_{tpc}+\kappa_{tpd}}{\kappa_{ppc}+2\kappa_{ppd}}$. Depending on M, several distinct regimes of behavior can be identified:

(1) $\mathrm{M} > 1$: the trace component is displaced further from the wall than the primary component: it *demarginates*.

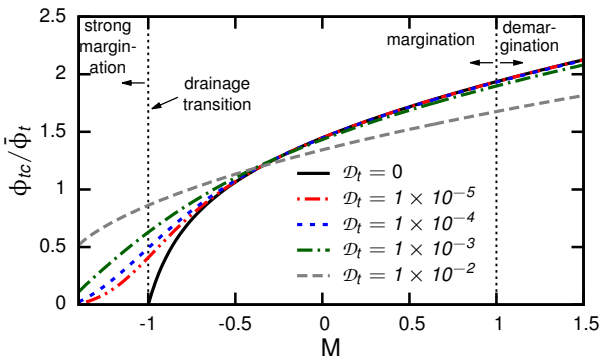

FIG. 6. Centerline volume fraction of the trace component ϕ_{tc} scaled with the average trace volume fraction $\bar{\phi}_t$ *vs.* M for varying $\mathcal{D}_t$. Other parameters are the same as in Fig. 5.

(2) $0 < \mathrm{M} < 1$: the relative concentration of the trace component is higher near the wall than the primary component but does not display a peak: it *weakly marginates*.

(3) $-1 < \mathrm{M} < 0$: the trace component displays a peak at $y = l_d$, corresponding to an integrably singular concentration profile: it *moderately marginates*.

(4) $\mathrm{M} \leq -1$: here Eq. 55 displays a nonintegrable singularity at $y = l_d$. This steady state is physically unrealizable as it corresponds to an infinite amount of material in a finite region. In this regime collisional transport overwhelms migration, and the trace component accumulates indefinitely at $y = l_d$, indicating *strong margination*.

The black solid line in Fig. 6 shows the ratio between the centerline concentration ϕ_{tc} and the average concentration $\bar{\phi}_t$ *vs.* M. This falls sharply to zero at $\mathrm{M} = -1$; we call this phenomenon the *drainage transition*, since for $\mathrm{M} \leq -1$ all the trace component is completely drained from the bulk. If the trace component does not migrate (as in the case of rigid particles), then $\kappa_{tm} = 0$ and $\mathrm{M} = -(1 + \kappa_{tc}/\kappa_{td})$, which is *always* less than -1. This case is degenerate in the absence of Brownian diffusion, because at steady state ϕ_t can take on arbitrary values when $y < l_d$. In the case of shape segregation, Sinha and Graham [63] have used simulations of pair collisions and single-particle migration to estimate M via computation of the κ parameters in Eq. 56.

For particles the size of blood cells ($> 1\mu m$) at shear rates characteristic of the microcirculation ($10^2 - 10^3\ s^{-1}$), Brownian diffusion is unimportant – using typical values for the microcirculation, the Péclet number (Pe) is about 10^5. For smaller particles, however, such as might be used for drug delivery, this may no longer be true. We consider the impact

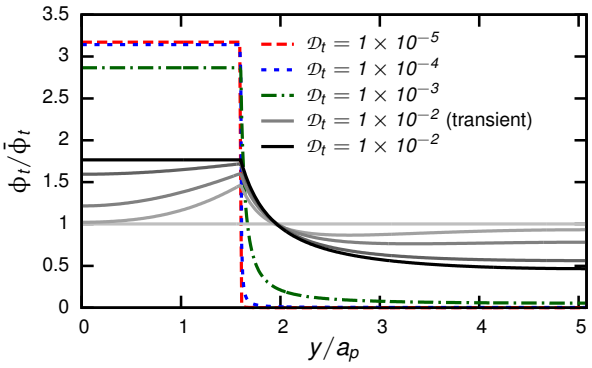

FIG. 7. Steady state volume fraction profiles $\phi_t(y)/\bar{\phi}_t$ for $\kappa_{tm} = 0$ (M < -1) and various $\mathcal{D}_t$. Other parameters are the same as in Fig. 5. Also, the solid lines show the transient evolution for $\mathcal{D}_t = 1 \times 10^{-2}$: $t = 0$ (lightest gray), 30, 90, 270, and at steady state (black).

of Brownian diffusion on trace component transport by adding the appropriately nondimensionalized diffusion term $\mathcal{D}_t\ \partial^2\phi_t/\partial y^2$ in Eq. 28 for $\alpha = t$. Here $\mathcal{D}_t = D_t/a_p^2\dot{\gamma}$, where D_t is the Brownian diffusivity of the trace component. Note that $\mathcal{D}_t$ is a measure of the competition between diffusive and convective transport, since it is inversely proportional to Pe: $\mathcal{D}_t = \mathrm{S}^2/\mathrm{Pe}$. Using typical values for blood ($a_p = 3.9 \times 10^{-6}$ m, $\dot{\gamma} = 500\ \mathrm{s}^{-1}$) and the Stokes-Einstein relation, varying $\mathcal{D}_t$ from 10^{-5} to 10^{-2} corresponds to varying a_t from $\sim 10^{-6}$ m to $\sim 10^{-9}$m.

With molecular diffusion the steady solution for the trace component is

$$\phi_t = \begin{cases} \phi_{tc}\left(1 - \frac{2\eta_p\kappa_{tpd}}{\mathrm{C}(\mathcal{D}_t+\phi_{pc}\kappa_{tpd})}\frac{(\mathrm{C}-l_d)^2}{l_d(2\mathrm{C}-l_d)}\right)^{\mathrm{M}} \\ \times \exp\left(-\frac{2\kappa_{tm}\mathrm{C}}{\mathcal{D}_t}\left(\frac{1}{y(2\mathrm{C}-y)} - \frac{1}{l_d(2\mathrm{C}-l_d)}\right)\right), & y < l_d \\ \phi_{tc}\left(1 - \frac{2\eta_p\kappa_{tpd}}{\mathrm{C}(\mathcal{D}_t+\phi_{pc}\kappa_{tpd})}\frac{(\mathrm{C}-y)^2}{y(2\mathrm{C}-y)}\right)^{\mathrm{M}}, & y > l_d. \end{cases} \tag{57}$$

Molecular diffusion results in a spreading of ϕ_t to include the region $y < l_d$ and also renders the steady solution for M ≤ -1 integrable. Fig. 6 shows the volume fraction of the trace component at the centerline ϕ_{tc} normalized with $\bar{\phi}_t$ as a function of M for various $\mathcal{D}_t$. It shows that the drainage transition (*i.e.*, the value of M at which there is a complete drainage of the trace component from the bulk) is smeared out by the addition of molecular diffusion.

Now consider the specific case in which the particles of the trace component are rigid ($\kappa_{tm} = 0$). Fig. 7 shows how the steady state profile of ϕ_t varies with $\mathcal{D}_t$: Margination is weakened by diffusion. This result is consistent with experimental [13] and numerical [77] studies in which nanoparticles, which experience a stronger molecular diffusion, showed a

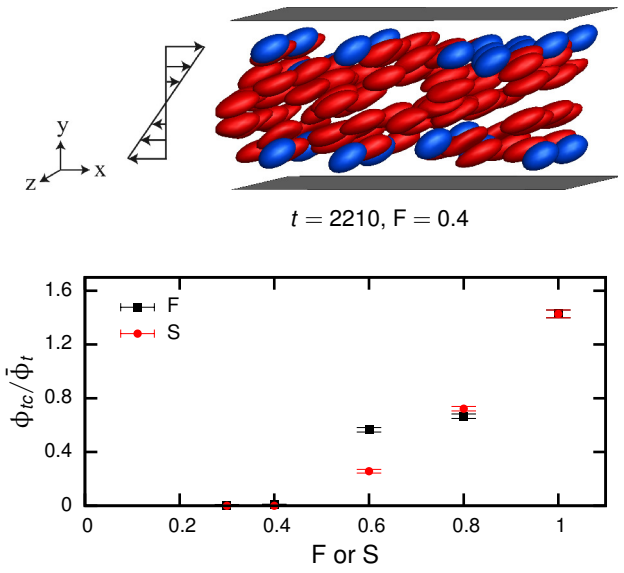

FIG. 8. Time-averaged volume fraction, based on center-of-mass position, of the trace components at the centerline as a function of flexibility ratio F or size ratio S from direct hydrodynamic simulations, where C = 5.08 and $\bar{\phi} = 0.12$ in case (a) and $\bar{\phi} = \{0.096, 0.098, 0.101, 0.108, 0.12\}$ for S $= \{0.2, 0.4, 0.6, 0.8, 1.0\}$ in case (b). The value of l_d is 1.6.

lower margination than microparticles. Fig. 7 also shows the transient evolution of ϕ_t for $\mathcal{D}_t = 1 \times 10^{-2}$ from a uniform initial condition as determined from a numerical simulation using a conservative finite volume method.

To evaluate the prediction of a drainage transition, we performed direct simulations of binary suspensions of fluid-filled non-Brownian elastic capsules at low Reynolds number using a boundary integral method. For more information about simulation methods and details consult [20, 22, 72]. Two cases were considered: segregation by (a) deformability and (b) size. The particles are all spherical at rest. In case (a) the primary component comprises 80% of the particles and has $\mathrm{Ca}_p = 0.5$; the trace component is stiffer, and we define a flexibility ratio $\mathrm{F} = G_p/G_t$ ($= \mathrm{Ca}_t/\mathrm{Ca}_p$ in our simulations). The primary component in case (b) is the same as in case (a), but now the trace component is smaller as defined by the size ratio $\mathrm{S} = a_t/a_p$. In this case $\mathrm{Ca}_t = \mathrm{Ca}_p$.

Fig. 8 shows the steady-state value of $\phi_{tc}/\bar{\phi}_t$ as F or S changes, where the values of volume fraction are based on center-of-mass position. It is very similar to Fig. 6, clearly indicating that the drainage transition predicted by theory is found in the simulations. Coincidentally, the transition is in the same range $0.4 - 0.6$ for both S and F under the conditions chosen.

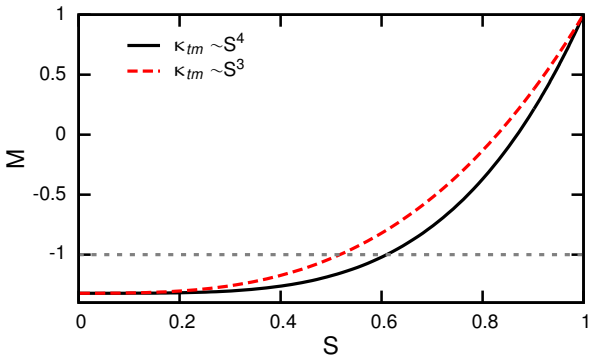

FIG. 9. M *vs.* S for $\kappa_{tm} \sim \mathrm{S}^4$ (black solid line) and $\kappa_{tm} \sim \mathrm{S}^3$ (red dashed line); the latter corresponds to the simulations shown in Fig. 8. Other parameters are the same as in Fig.5.

Considering case (b) first, the migration parameter κ_{tm} scales as S^3 at constant Ca_t, so as S decreases so does M; recall that $\mathrm{M} < -1$ for $\kappa_{tm} = 0$. With regard to case (a), κ_{tm} also decreases with decreasing F, and additionally the collisional displacements and thus κ_{tpc} and κ_{tpd} increase [20]. Therefore, decreasing F also corresponds to decreasing M, resulting in a drainage transition.

Returning to the theory, using the values in the caption of Fig. 5 and Eq. 56, we can determine the value of S corresponding to the drainage transition by finding M as S is varied. This result is shown in Fig. 9, where we use $\kappa_{tm} \sim \mathrm{S}^4$ (black solid line) and $\kappa_{tm} \sim \mathrm{S}^3$ (red dashed line) to represent the cases of varying a_t while keeping G_t and Ca_t constant, respectively. The values of S corresponding to the drainage transition are 0.61 and 0.52, respectively. The latter case corresponds to case (b) above, and we see that the theory result agrees well with the direct simulation result in Fig. 8.

For reference to blood in the microcirculation, the values of S for leukocytes and platelets with respect to RBCs are $0.9-2$ [78] and 0.2 [79] respectively, while F is of the order 10^{-2} [80] and 10^{-4} [81] respectively. Thus, case (a) here is more closely related to the RBC-leukocyte segregation, where the size ratio is close to unity, and case (b) more nearly represents the RBC-platelet case, where the sizes are very different. From the present results it appears that both leukocytes and platelets would satisfy the conditions for drainage in simple shear.

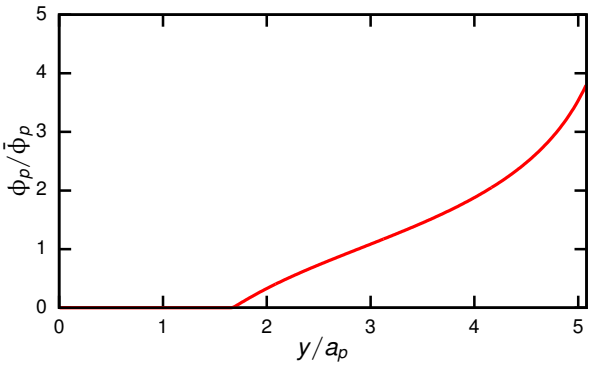

FIG. 10. Steady state ϕ_p profile normalized with $\bar{\phi}_p$ for Poiseuille flow. Here $\bar{\phi}_p = 0.2$, C = 5.08, $\kappa_w = 0.15$, $\kappa_{sg} = 0.01$, $\kappa_1 = 0.16$, $\kappa_{ppc} = 0.02$, $\kappa_{ppd} = 0.07$, $\kappa'_{pc} = 0.02$, $\kappa'_{pd} = 0.07$, $\mathcal{D}_p = 0$, and $\kappa_{pe} = 0$.

B. Poiseuille Flow

Now we present results of the drift-diffusion model for plane Poiseuille flow (Eq. 49). Again, unless otherwise noted, wall exclusion and molecular diffusion are neglected. Here analytical solutions are not available, but the pair of differential equations represented by Eq. 49 can be solved numerically using a conservative finite volume method. The steady-state solution of the primary is shown in Fig. 10. It has a distinctive peak at the centerline, which is not observed in the simple shear flow case. The solution of ϕ_p at the centerline is finite due to the presence of the κ'_{pc} and κ'_{pd} terms in Eq. 49; otherwise it would blow up. The same is true about the solution of the trace component. The peak at the centerline in the solution of the primary component has been observed in experiments with rigid-sphere suspensions [82] as well as in simulations of suspensions of RBCs [83] and deformable fluid-filled spherical capsules [84]. For comparison with the theory, Fig. 11 shows $\phi_p/\bar{\phi}_p$ as a function of y from boundary integral simulations of suspensions of fluid-filled elastic capsules at low Reynolds number (*cf.* [20, 22, 72]), where the values of volume fraction are based on center-of-mass position. In the boundary integral simulations, $\mathrm{Ca}_p = 0.5$ and C = 5.08. As in the Couette flow case, Fig. 11 shows that the primary component also exhibits a peak close to the cell-free layer, which our local theory is not able to capture. As noted above, in Couette flow this peak is captured by the nonlocal theory presented by Kumar *et al.* [22].

Steady-state solutions for the trace component (Eq. 49) are shown as the solid lines in

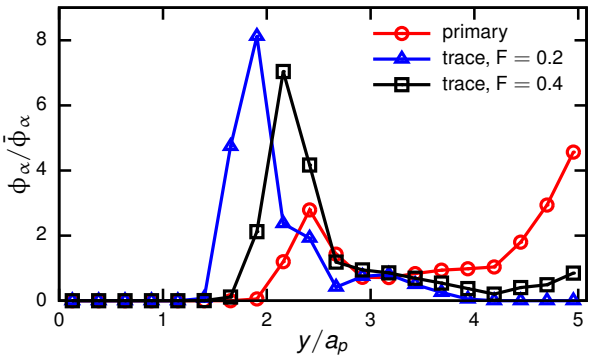

FIG. 11. Steady state ϕ_α profiles normalized with $\bar{\phi}_\alpha$ for Poiseuille flow from direct simulations. Here the values of volume fraction are based on center-of-mass position, $\bar{\phi} = 0.12$, $\mathrm{Ca}_p = 0.5$, $\mathrm{C} = 5.08$, and F is varied by changing Ca_t.

Fig. 12 for different values of the wall margination parameter M_w, where

$$\begin{aligned}\mathrm{M}_w &= \frac{\kappa_{ppc}+2\kappa_{ppd}}{\kappa_{tpd}}\left(\frac{\kappa_{tm}}{\kappa_{pm}}-\frac{\kappa_{tpc}+\kappa_{tpd}}{\kappa_{ppc}+2\kappa_{ppd}}\right)\\ &= \frac{\kappa_{ppc}+2\kappa_{ppd}}{\kappa_{tpd}}\left(\frac{\mathrm{Ca}_t}{\kappa_1+\mathrm{Ca}_t}\frac{\kappa_1+\mathrm{Ca}_p}{\mathrm{Ca}_p}-\frac{\kappa_{tpc}+\kappa_{tpd}}{\kappa_{ppc}+2\kappa_{ppd}}\right).\end{aligned} \tag{58}$$

As its name suggests, M_w is simply M (Eq. 56) evaluated at the wall. The contribution of the shear gradient to migration is neglected in this characterization as it is assumed to be small compared to the wall-induced migration near the wall. Near the wall, the solution of the trace is qualitatively similar to that in the simple shear flow case; near the centerline we also find a peak like that exhibited by the primary component. The same qualitative margination regimes are also observed:

(1) $\mathrm{M}_w > 1$: the trace *demarginates*.

(2) $0 < \mathrm{M}_w < 1$: the trace *weakly marginates*.

(3) $-1.3 \lesssim \mathrm{M}_w < 0$: the trace *moderately marginates*. In this margination regime, two peaks in the volume fraction profile of the trace form: one at the centerline and another at $y = l_d$.

(4) $\mathrm{M}_w \lesssim -1.3$, as shown below: Eq. 49 for $\alpha = t$ displays a nonintegrable singularity at $y = l_d$, indicating *strong margination*.

The (small) effect of molecular diffusion of the trace component is also shown in Fig. 12.

As in simple shear flow, we predict a complete drainage of the trace from the bulk. This is shown in Fig. 13 where the steady state value of ϕ_{tc} normalized with $\bar{\phi}_t$ is plotted against

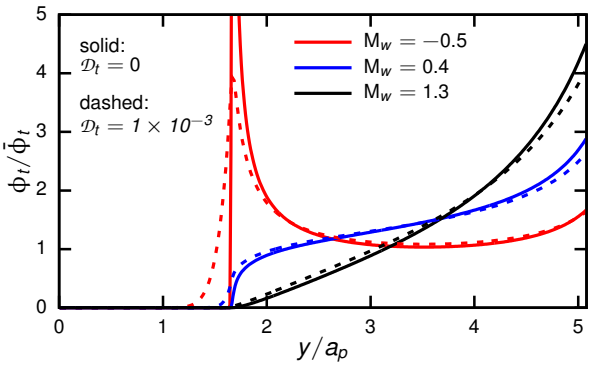

FIG. 12. Steady state ϕ_t profiles for different values of M_w in Poiseuille flow for $\mathcal{D}_t = 0$ (solid lines) and $\mathcal{D}_t = 1 \times 10^{-3}$ (dashed lines). Here C = 5.08, $\bar{\phi}_p = 0.2$, $Ca_p = 0.5$, $\kappa_w = 0.15$, $\kappa_{sg} = 0.01$, $\kappa_1 = 0.16$, $\kappa_{ppc} = 0.02$, $\kappa_{ppd} = 0.07$, $\mathcal{D}_p = 0$, $\kappa_{pe} = 0$, and $\kappa_{te} = 0$. For simplicity, $\kappa'_{pc} = \kappa_{tpc} = \kappa'_{tc} = \kappa_{ppc}$ and $\kappa'_{pd} = \kappa_{tpd} = \kappa'_{td} = \kappa_{ppd}$. We vary M_w by changing Ca_t.

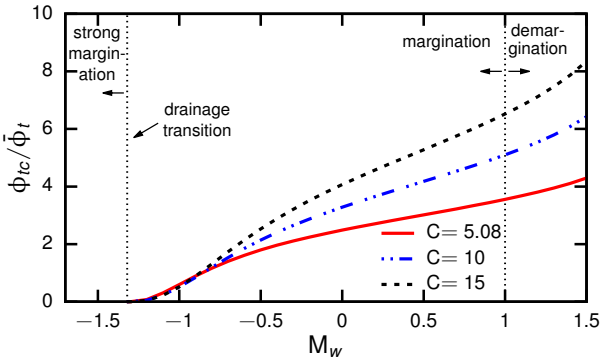

FIG. 13. Steady-state value of $\phi_{tc}/\bar{\phi}_t$ *vs.* M_w in Poiseuille flow for various C. Other parameters are the same as in Fig. 12.

M_w for various C. For all the values of C shown, a complete drainage can be observed for $M_w \lesssim -1.3$, meaning that the drainage transition occurs at $M_w \approx -1.3$.

As in the simple shear flow case, we can evaluate the prediction of a drainage transition in Poiseuille flow by performing direct simulations of fluid-filled non-Brownian elastic capsules at low Reynolds number (*cf.* [20, 22, 72]). We consider segregation by deformability. Recall that in Poiseuille flow $Ca_\alpha = \mu\dot{\gamma}_w a_\alpha/G_\alpha$. The primary component comprises 80% of the particles and has $Ca_p = 0.5$. The flexibility ratio F was varied by changing Ca_t. Recall that the flexibility ratio between the capsules is $F = G_p/G_t$ ($= Ca_t/Ca_p$ in our simulations).

Fig. 14 shows direct simulation results for the steady-state value of $\phi_{tc}/\bar{\phi}_t$ as F is varied.

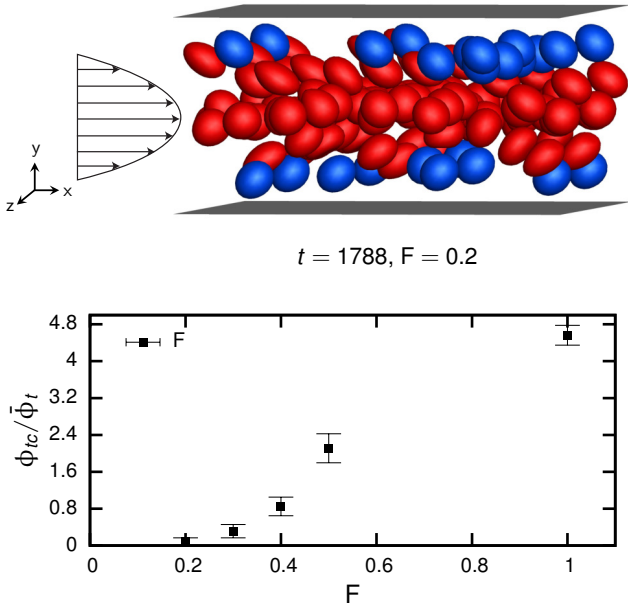

FIG. 14. Time-averaged volume fraction, based on center-of-mass position, of the trace components at the centerline as a function of flexibility ratio F from direct hydrodynamic simulations, where C = 5.08 and $\bar{\phi} = 0.12$. The value of l_d is 1.8.

As in the simple shear flow case, ϕ_{tc} decreases with decreasing F, and a complete drainage of the trace from the bulk is observed at F $\approx$ 0.2, supporting the prediction by the theory. Fig. 11 shows the volume fraction profiles for F = 0.4 and 0.2. The latter profile explicitly shows the absence of capsules in the region near the channel centerline.

Up to this point only steady state results have been presented. Here we briefly turn to the transient development of the steady state concentration profiles, focusing on the Poiseiulle flow case. To provide an overview of the parameter dependence of the transient development, we have performed transient simulations for several values of M_w at C = 10, 15, 20, and 40, starting from a uniform concentration profile and determined the time t_{ss} required to reach steady state (to within a given tolerance as measured with the L_2 norm of the number density profiles). For each M_w, we then found the best fit of t_{ss} *vs.* C to a power law $t_{ss} = aC^b$. The exponents b of the power law fits are plotted against M_w in Fig. 15. The red triangle represents the special case of a monodisperse suspension of rigid particles, for which there is no hydrodynamic migration. In this case $t_{ss} \sim C^2$. This is diffusive scaling and is expected since the only mechanism of cross-stream transport is shear-induced collisions. It agrees with previously presented results for suspensions of rigid particles in pressure-driven

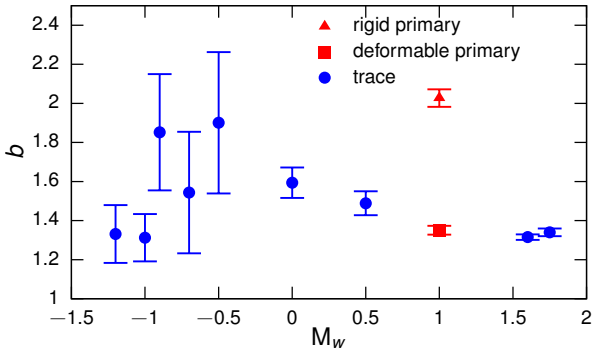

FIG. 15. Exponent b from the best fit of t_{ss} *vs.* C, from transient simulations, to a power law $t_{ss} = a\mathrm{C}^b$ as a function of M_w. The values of C used in the transient simulations for the fits are 10, 15, 20, and 40. The red square represents the primary component (or the trace component for $\mathrm{M}_w = 1$). The blue circles represent the trace component for various values of M_w. The red triangle represents the primary component in the special case in which the particles of the primary component have a zero migration velocity (*e.g.*, rigid particles). The large error bars for $\mathrm{M}_w < 0$ represent poor fit to a power law. In the transient simulations, the initial condition is a uniform concentration profile, $\bar{\phi}_p = 0.2$, $\kappa_{ppc} = 0.02$, $\kappa_{ppd} = 0.07$, $\mathcal{D}_p = 0$, $\mathcal{D}_t = 0$, $\kappa_{pe} = 0$, and $\kappa_{te} = 0$. For simplicity, $\kappa'_{pc} = \kappa_{tpc} = \kappa'_{tc} = \kappa_{ppc}$ and $\kappa'_{pd} = \kappa_{tpd} = \kappa'_{td} = \kappa_{ppd}$. We vary M_w by changing Ca_t. Additionally, the parameters related to migration are $\mathrm{Ca}_p = 0.5$, $\kappa_w = 0.15$, $\kappa_1 = 0.16$, and $\kappa_{sg} = 0.01$, except for the rigid primary case in which the migration velocity is zero.

flow [45]. Now we examine the time scaling for suspensions whose primary component is deformable. The red square represents the primary component, as well as the trace component for $\mathrm{M}_w = 1$. For this case $t_{ss} \sim \mathrm{C}^{1.4}$. The blue circles represent results for the trace component for various values of M_w. There is no observable power law between t_{ss} and C for negative M_w, as shown by the large error bars associated with attempting a power law fit. However, for $\mathrm{M}_w \gtrsim 0$ the results fit a power law very well. The values of b are approximately 1.35-1.6. We do not as yet have a simple theory to explain these results.

C. Effect of Volume Fraction on cell-free layer and margination

As mentioned in Sec. I, studies have yet to agree on the effect of Hct (mean volume fraction $\bar{\phi}_p$) on margination of white blood cells. We present a hypothesis regarding this

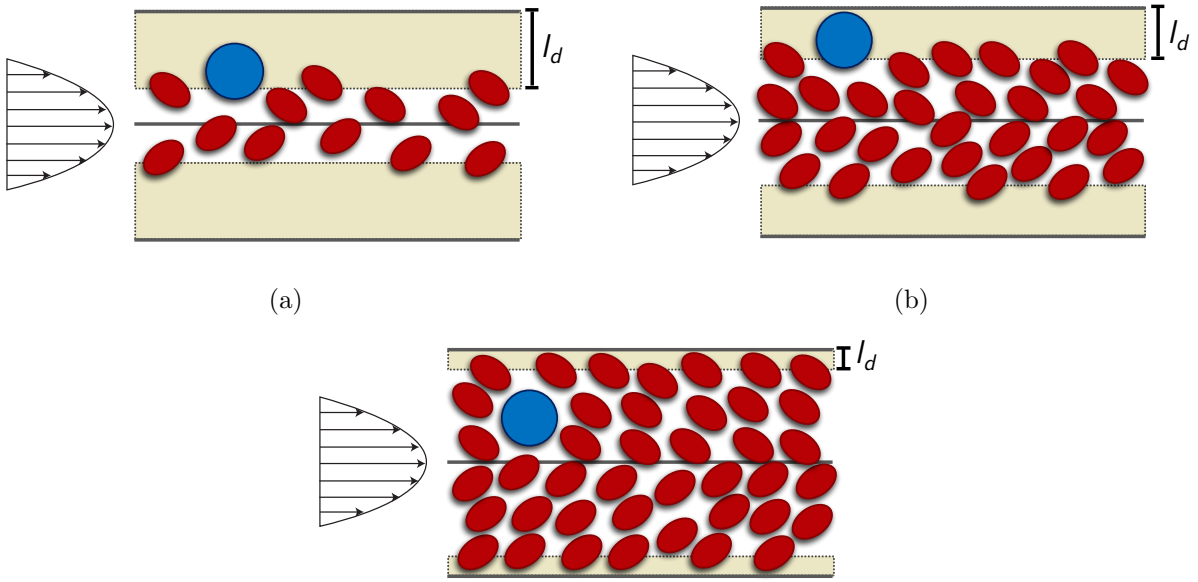

(a) (b)

(c)

FIG. 16. Schematic of a suspension of trace particles, white blood cells (blue spheres), and primary particles, red blood cells (red ellipses), for different ranges of $\bar{\phi}_p$ (*i.e.*, hematocrit): (a) limit of small $\bar{\phi}_p$, (b) intermediate values of $\bar{\phi}_p$, and (c) limit of large $\bar{\phi}_p$.

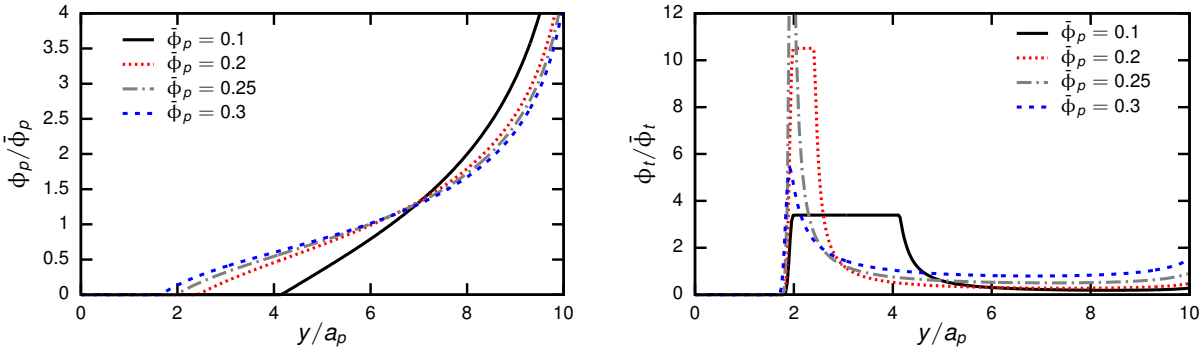

(a) (b)

FIG. 17. Steady state volume fraction profiles of (a) $\phi_p/\bar{\phi}_p$ and (b) $\phi_t/\bar{\phi}_t$ for various $\bar{\phi}_p$. Here C = 10, $\kappa_w = 0.15$, $\kappa_{sg} = 0.01$, $\kappa_1 = 0.16$, $\kappa_{ppc} = 0.04$, $\kappa_{ppd} = 0.14$, $\mathcal{D}_p = 0$, $\mathcal{D}_t = 1 \times 10^{-3}$, $\kappa_{pe} = 5.2$, $\kappa_{te} = 2.6$, and S = 2. For simplicity, $\kappa'_{pc} = \kappa_{tpc} = \kappa'_{tc} = \kappa_{ppc}$ and $\kappa'_{pd} = \kappa_{tpd} = \kappa'_{td} = \kappa_{ppd}$.

effect and predictions by the theory that support the hypothesis. See Fig. 16 for a schematic for reference as we describe the hypothesis. We present three regimes for the effect of Hct: (a) the limit of low Hct, (b) intermediate values of Hct, and (c) the limit of high Hct. In regime (a), l_d is large and WBCs are not confined to a small region near the wall. WBCs

have a larger distance they can move along the wall-normal direction without being pushed toward the wall by frequent collisions with RBCs. Thus WBC margination in this regime is weak. In the other extreme case, regime (c), l_d is very small, in particular it is smaller than than the radius of the WBCs. In this regime, WBCs experience collisions from RBCs whose centers of mass are closer to the wall than theirs, keeping WBCs from staying confined to a small region near the wall. Thus, margination is also weak in this regime. Lastly, in regime (b), l_d is smaller than in case (a) but still larger than the radius of a WBC. Here WBCs experience frequent collisions with RBCs and marginate normally.

To address this hypothesis we consider the effect of volume fraction of the primary component on margination in a binary suspension of deformable primary particles (RBCs) and larger rigid trace particles (WBCs) with $v_{tm} = 0$. Most importantly, we now include wall volume exclusion flux terms for both the primary and trace components to account for the finite particle sizes in the near-wall region. For the wall exclusion we take S = 2, corresponding to WBCs that are twice the radius of RBCs. We also include a small molecular diffusivity for the trace component to avoid the degenerate situation mentioned in Sec.III A, in which ϕ_t can take on arbitrary values when $y < l_d$ and $v_{tm} = 0$. The collision parameters in the caption of Fig. 17 are used, in which case $\mathrm{M}_w = -1.3$.

Figs. 17(a) and 17(b) show volume fraction profiles as $\bar{\phi}_p$ increases. The depletion layer thickess l_d decreases with increasing $\bar{\phi}_p$. For $\bar{\phi}_p \lesssim 0.25$, the degree of margination of the trace particles increases with increasing $\bar{\phi}_p$, resulting in a sharp peak for the trace component at $\bar{\phi}_p = 0.25$. However, as $\bar{\phi}_p$ increases further, l_d becomes smaller than the size (S = 2) of the trace component: the primary component is closer to the wall than the excluded volume term allows the trace component to be. Accordingly, margination is strongly suppressed at high $\bar{\phi}_p$, confirming the hypothesis we posed above. Interestingly, although the height of the near-wall peak in ϕ_t is nonmonotonic in $\bar{\phi}_p$, the peak at the centerline is monotonically increasing with $\bar{\phi}_p$.

Finally, we note that in the present model, nothing prevents the volume fraction from exceeding a maximum value. For example the centerline value of ϕ_p is unrealistically large at ≈ 0.9 when $\bar{\phi}_p = 0.3$. Future developments of this model will need to incorporate the physical phenomena of volume exclusion and increase in viscosity as the volume fraction becomes large.

IV. CONCLUSIONS

A mechanistic model, derived from kinetic theory, has been developed to describe flow-induced segregation phenomena in multicomponent suspensions such as blood. Migration, shear-induced diffusion, volume exclusion near the wall, and Brownian diffusion are incorporated in the model. Two flow profiles are considered: (a) simple shear flow and (b) Poiseuille flow. The model captures key phenomena that are observed experimentally and computationally such as cell-free layer formation and margination.

In the case of simple shear flow, closed-form solutions are available. The expression for cell-free layer thickness takes the form of a master curve with one free parameter and can be fit remarkably well to results from various sources (experiments, detailed simulations, theory) with different parameters (flexibility of different components in the suspension, viscosity ratio, confinement, among others). More generally, the form of the master curve is independent of the theory and set by only one adjustable parameter. In multicomponent suspensions several different segregation regimes arise as determined by a single "margination parameter" that emerges from the theory. If this parameter is sufficiently negative, a sharp drainage transition is identified beyond which the trace component of the suspension partitions completely to the edge of the cell-free layer. Direct simulations corroborate this prediction.

In plane Poiseuille flow analytical solutions are not available so numerical solutions are found. Cell-free layer behavior and margination regimes are found to be qualitatively similar to those in the simple shear case. A drainage transition is also observed but is shifted to a more negative value of the margination parameter. Direct simulations also corroborate the existence of a drainage transition. Moreover, the time for development of the steady-state profiles has been examined. Power law scaling is observed only for positive values of the margination parameter. Furthermore, a hypothesis has been presented to describe the effect of hematocrit on margination in blood flow as observed in some prior studies. Results from the theory support the hypothesis.

The framework presented here can be extended in many directions. For example, suspensions of three components can be studied, which would be more akin to blood in microfluidic and circulatory applications, where the three components could be red blood cells, white blood cells, and platelets. A case in which the values of n_t and n_p are comparable can also be

studied by using the fully coupled version of Eq. 18 in which the pair collisions with particles of component α are also considered. The model can be extended phenomenologically to include many other phenomena, including finite volume fraction effects and platelet adhesion. For example, red blood cell aggregation can be included by adding the flux associated with a volume-fraction-dependent potential with a minimum in volume fraction. Effects of increasing volume fraction can be modeled by incorporating a volume-fraction-dependent viscosity and solving the momentum equation along with the drift-diffusion equations to capture the interaction between velocity profile and volume fraction distribution. Furthermore, the same potential that can be used to model aggregation can be used to model excluded volume between cells by making the potential diverge as a maximum volume fraction is approached. Platelet adhesion can be incorporated by adding the flux corresponding to an attractive potential at the wall. Most importantly, the theory provides substantial insights into the mechanisms of margination and flow-induced segregation phenomena.

ACKNOWLEDGMENTS

This material is based upon work supported by the National Science Foundation under Grants No. CBET-1132579 and No. CBET-1436082 and a National Science Foundation Graduate Research Fellowship Program under Grant No. DGE-1256259 awarded to RH.

V. REFERENCES

[1] Matthias E Möbius, Benjamin E Lauderdale, Sidney R Nagel, and Heinrich M Jaeger, "Brazil-nut effect: Size separation of granular particles," Nature **414**, 270–270 (2001).

[2] M Makino and M Sugihara-Seki, "Segregation by size difference in binary suspensions of fluid droplets in channel flow," Biorheology **50**, 149–163 (2013).

[3] Hadi Mohammadigoushki and James J Feng, "Size Segregation in Sheared Two-Dimensional Polydisperse Foam," Langmuir **29**, 1370–1378 (2013).

[4] S P Sutera and R Skalak, "The history of Poiseuille's law," Annu. Rev. Fluid Mech. **25**, 1–19 (1993).

[5] GJ Tangelder, Harry C Teirlinck, Dick W Slaaf, and Robert S Reneman, "Distribution of blood platelets flowing in arterioles," Am. J. Physiol.: Heart Circ. Physiol. **248**, H318–H323 (1985).

[6] John C Firrell and Herbert H Lipowsky, "Leukocyte margination and deformation in mesenteric venules of rat," Am. J. Physiol.: Heart Circ. Physiol. **256**, H1667–H1674 (1989).

[7] A S Popel and P C Johnson, "Microcirculation and hemorheology," Annu. Rev. Fluid Mech. **37**, 43–69 (2005).

[8] Amit Kumar and Michael D Graham, "Margination and segregation in confined flows of blood and other multicomponent suspensions," Soft Matter **8**, 10536–10548 (2012).

[9] Xavier Grandchamp, Gwennou Coupier, Aparna Srivastav, Christophe Minetti, and Thomas Podgorski, "Lift and down-gradient shear-induced diffusion in red blood cell suspensions," Phys. Rev. Lett. **110**, 108101 (2013).

[10] Han Wei Hou, Hiong Yap Gan, Ali Asgar S Bhagat, Leon D Li, Chwee Teck Lim, and Jongyoon Han, "A microfluidics approach towards high-throughput pathogen removal from blood using margination," Biomicrofluidics **6**, 024115 (2012).

[11] Han Wei Hou, Lidan Wu, Diana P Amador-Munoz, Miguel Pinilla Vera, Anna Coronata, Joshua A Englert, Bruce D Levy, Rebecca M Baron, and Jongyoon Han, "Broad spectrum immunomodulation using biomimetic blood cell margination for sepsis therapy," Lab Chip (2016).

[12] Katawut Namdee, Alex J Thompson, Phapanin Charoenphol, and Omolola Eniola-Adefeso, "Margination propensity of vascular-targeted spheres from blood flow in a microfluidic model of human microvessels," Langmuir **29**, 2530–2535 (2013).

[13] Alex J Thompson, Eric M Mastria, and Omolola Eniola-Adefeso, "The margination propensity of ellipsoidal micro/nanoparticles to the endothelium in human blood flow," Biomaterials **34**, 5863–5871 (2013).

[14] David Boal, *Mechanics of the Cell*, 2nd ed. (Cambridge University Press, Cambridge, 2012).

[15] Bruce Alberts, Alexander Johnson, Julian Lewis, Martin Raff, Keith Roberts, and Peter Walter, *Molecular Biology of the Cell*, 5th ed. (Garland Science, New York, 2007).

[16] Harry L Goldsmith and Samira Spain, "Margination of leukocytes in blood flow through small tubes," Microvasc. Res. **27**, 204–222 (1984).

[17] MJ Pearson and HH Lipowsky, "Influence of erythrocyte aggregation on leukocyte margination in postcapillary venules of rat mesentery," Am. J. Physiol.: Heart Circ. Physiol. **279**, H1460–H1471 (2000).

[18] Katherine B Abbitt and Gerard B Nash, "Rheological properties of the blood influencing selectin-mediated adhesion of flowing leukocytes," Am. J. Physiol.: Heart Circ. Physiol. **285**, H229–H240 (2003).

[19] Meredith E Fay, David R Myers, Amit Kumar, Cory T Turbyfield, Rebecca Byler, Kaci Crawford, Robert G Mannino, Alvin Laohapant, Erika A Tyburski, Yumiko Sakurai, *et al.*, "Cellular softening mediates leukocyte demargination and trafficking, thereby increasing clinical blood counts," Proc. Natl. Acad. Sci. U. S. A. **113**, 1987–1992 (2016).

[20] Amit Kumar and Michael D Graham, "Segregation by membrane rigidity in flowing binary suspensions of elastic capsules," Phys. Rev. E **84**, 066316 (2011).

[21] Amit Kumar and Michael D Graham, "Mechanism of margination in confined flows of blood and other multicomponent suspensions," Phys. Rev. Lett. **109** (2012).

[22] Amit Kumar, Rafael G Henríquez Rivera, and Michael D Graham, "Flow-induced segregation in confined multicomponent suspensions: Effects of particle size and rigidity," J. Fluid Mech. **738**, 423–462 (2014).

[23] Chenghai Sun, Cristiano Migliorini, and Lance L Munn, "Red blood cells initiate leukocyte rolling in postcapillary expansions: a lattice Boltzmann analysis," Biophys. J. **85**, 208–222 (2003).

[24] Jonathan B Freund, "Leukocyte margination in a model microvessel," Phys. Fluids **19**, 023301 (2007).

[25] Dmitry A Fedosov, Julia Fornleitner, and Gerhard Gompper, "Margination of white blood cells in microcapillary flow," Phys. Rev. Lett. **108**, 028104 (2012).

[26] Dmitry A Fedosov and Gerhard Gompper, "White blood cell margination in microcirculation," Soft Matter **10**, 2961–2970 (2014).

[27] B Woldhuis, GJ Tangelder, Dick W Slaaf, and Robert S Reneman, "Concentration profile of blood platelets differs in arterioles and venules," Am. J. Physiol.: Heart Circ. Physiol. **262**, H1217–H1223 (1992).

[28] Arno W Tilles and Eugene C Eckstein, "The near-wall excess of platelet-sized particles in blood flow: its dependence on hematocrit and wall shear rate," Microvasc. Res. **33**, 211–223

(1987).

[29] E C Eckstein, A W Tilles, and F J Millero, "Conditions for the occurrence of large near-wall excess of small particles during blood flow," Microvasc. Res. **36**, 31–39 (1988).

[30] PA Aarts, SA Van Den Broek, Gerrit W Prins, GD Kuiken, Jan J Sixma, and Robert M Heethaar, "Blood platelets are concentrated near the wall and red blood cells, in the center in flowing blood." Arterioscler., Thromb., Vasc. Biol. **8**, 819–824 (1988).

[31] WS Uijttewaal, EJ Nijhof, PJ Bronkhorst, Emiel Den Hartog, and Robert M Heethaar, "Near-wall excess of platelets induced by lateral migration of erythrocytes in flowing blood," Am. J. Physiol.: Heart Circ. Physiol. **264**, H1239–H1244 (1993).

[32] Chinjung Yeh and Eugene C Eckstein, "Transient lateral transport of platelet-sized particles in flowing blood suspensions." Biophys. J. **66**, 1706 (1994).

[33] Sean Fitzgibbon, Andrew P Spann, Qin M Qi, and Eric S G Shaqfeh, "In vitro measurement of particle margination in the microchannel flow: Effect of varying hematocrit," Biophys. J. **108**, 2601–2608 (2015).

[34] T AlMomani, HS Udaykumar, JS Marshall, and KB Chandran, "Micro-scale dynamic simulation of erythrocyte–platelet interaction in blood flow," Ann. Biomed. Eng. **36**, 905–920 (2008).

[35] L Crowl and Aaron L Fogelson, "Analysis of mechanisms for platelet near-wall excess under arterial blood flow conditions," J. Fluid Mech. **676**, 348–375 (2011).

[36] Hong Zhao and Eric SG Shaqfeh, "Shear-induced platelet margination in a microchannel," Phys. Rev. E **83**, 061924 (2011).

[37] F Gadala-Maria and Andreas Acrivos, "Shear-induced structure in a concentrated suspension of solid spheres," J. Rheol. **24**, 799–814 (1980).

[38] Andrew L Zydney and Clark K Colton, "Augmented solute transport in the shear flow of a concentrated suspension," Physicochem. Hydrodyn. **10**, 77–96 (1988).

[39] David T Leighton and Andreas Acrivos, "The shear-induced migration of particles in concentrated suspensions," J. Fluid Mech. **181**, 415–439 (1987).

[40] R J Phillips, R C Armstrong, R A Brown, A L Graham, and J R Abbott, "A constitutive equation for concentrated suspensions that accounts for shear-induced particle migration," Phys. Fluids A **4**, 30–40 (1992).

[41] Philipp Kanehl and Holger Stark, "Hydrodynamic segregation in a bidisperse colloidal suspension in microchannel flow: A theoretical study," J. Chem. Phys. **142** (2015).

[42] MK Lyon and LG Leal, "An experimental study of the motion of concentrated suspensions in two-dimensional channel flow. part 2. bidisperse systems," J. Fluid Mech. **363**, 57–77 (1998).

[43] Anat Shauly, Amir Wachs, and Avinoam Nir, "Shear-induced particle migration in a polydisperse concentrated suspension," J. Rheol. **42**, 1329–1348 (1998).

[44] Denis Semwogerere and Eric R Weeks, "Shear-induced particle migration in binary colloidal suspensions," Phys. Fluids **20**, 043306 (2008).

[45] Prabhu R Nott and John F Brady, "Pressure-driven flow of suspensions: Simulation and theory," J. Fluid Mech. **275**, 157–199 (1994).

[46] Jeffrey F Morris and Fabienne Boulay, "Curvilinear flows of noncolloidal suspensions: The role of normal stresses," J. Rheol. **43**, 1213–1237 (1999).

[47] R M Miller and J F Morris, "Normal stress-driven migration and axial development in pressure-driven flow of concentrated suspensions," J. Non-Newtonian Fluid Mech. **135**, 149–165 (2006).

[48] Donald A Drew and Stephen L Passman, *Theory of multicomponent fluids*, Vol. 135 (Springer Science & Business Media, 2006).

[49] Jeffrey R Smart and David T Leighton Jr, "Measurement of the drift of a droplet due to the presence of a plane," Phys. Fluids A **3**, 21–28 (1991).

[50] Hongbo Ma and Michael D Graham, "Theory of shear-induced migration in dilute polymer solutions near solid boundaries," Phys. Fluids **17**, 083103 (2005).

[51] L. G. Leal, "Particle motions in a viscous fluid," Annu. Rev. Fluid Mech. **12**, 435–476 (1980).

[52] SD Hudson, "Wall migration and shear-induced diffusion of fluid droplets in emulsions," Phys. Fluids **15**, 1106–1113 (2003).

[53] P. C.-H. Chan and L. G. Leal, "The motion of a deformable drop in a second-order fluid," J. Fluid Mech. **92**, 131–170 (1979).

[54] Arun Ramachandran, Michael Loewenberg, and David T Leighton Jr, "A constitutive equation for droplet distribution in unidirectional flows of dilute emulsions for low capillary numbers," Phys. Fluids **22**, 083301 (2010).

[55] Pratik Pranay, Rafael G Henríquez Rivera, and Michael D Graham, "Depletion layer formation in suspensions of elastic capsules in newtonian and viscoelastic fluids," Phys. Fluids **24**, 061902 (2012).

[56] Vivek Narsimhan, Hong Zhao, and Eric SG Shaqfeh, "Coarse-grained theory to predict the concentration distribution of red blood cells in wall-bounded couette flow at zero reynolds number," Phys. Fluids **25**, 061901 (2013).

[57] Rafael G Henríquez Rivera, Kushal Sinha, and Michael D Graham, "Margination regimes and drainage transition in confined multicomponent suspensions," Phys. Rev. Lett. **114** (2015).

[58] Eugene C Eckstein and Fethi Belgacem, "Model of platelet transport in flowing blood with drift and diffusion terms." Biophys. J. **60**, 53 (1991).

[59] David L Bark and David N Ku, "Platelet transport rates and binding kinetics at high shear over a thrombus," Biophys. J. **105**, 502–511 (2013).

[60] Vijay Govindarajan, Vineet Rakesh, Jaques Reifman, and Alexander Y Mitrophanov, "Computational study of thrombus formation and clotting factor effects under venous flow conditions," Biophys. J. **110**, 1869–1885 (2016).

[61] FR Da Cunha and EJ Hinch, "Shear-induced dispersion in a dilute suspension of rough spheres," J. Fluid Mech. **309**, 211–223 (1996).

[62] M Zurita-Gotor, J Bławzdziewicz, and E Wajnryb, "Layering instability in a confined suspension flow," Phys. Rev. Lett. **108**, 068301 (2012).

[63] Kushal Sinha and Michael D Graham, "Shape-mediated margination and demargination in flowing multicomponent suspensions of deformable capsules," Soft Matter **12**, 1683–1700 (2016).

[64] Daniel A. Reasor, Marmar Mehrabadi, David N Ku, and Cyrus K Aidun, "Determination of critical parameters in platelet margination," Ann. Biomed. Eng. **41**, 238–249 (2013).

[65] Hong Zhao, Eric SG Shaqfeh, and Vivek Narsimhan, "Shear-induced particle migration and margination in a cellular suspension," Phys. Fluids **24**, 011902 (2012).

[66] Dmitry A Fedosov, Ming Dao, George Em Karniadakis, and Subra Suresh, "Computational biorheology of human blood flow in health and disease," Ann. Biomed. Eng. **42**, 368–387 (2013).

[67] Koohyar Vahidkhah, Scott L Diamond, and Prosenjit Bagchi, "Platelet dynamics in three-dimensional simulation of whole blood," Biophys. J. **106**, 2529–2540 (2014).

[68] X F Li and C Pozrikidis, "Wall-bounded shear flow and channel flow of suspensions of liquid drops," Int. J. Multiphase Flow **26**, 1247–1279 (2000).

[69] Crispin W Gardiner *et al.*, *Handbook of stochastic methods*, Vol. 3 (Springer Berlin, 1985).

[70] Dominique Barthès-Biesel, Anna Diaz, and Emmanuelle Dhenin, "Effect of constitutive laws for two-dimensional membranes on flow-induced capsule deformation," J. Fluid Mech. **460**, 211–222 (2002).

[71] Pratik Pranay, Samartha G Anekal, Juan P Hernández-Ortiz, and Michael D Graham, "Pair collisions of fluid-filled elastic capsules in shear flow: Effects of membrane properties and polymer additives," Phys. Fluids **22**, 123103 (2010).

[72] Amit Kumar and Michael D Graham, "Accelerated boundary integral method for multiphase flow in non-periodic geometries," J. Comput. Phys. **231**, 6682–6713 (2012).

[73] A Helmy and D. Barthès-Biesel, "Migration of a spherical capsule freely suspended in an unbounded parabolic flow," J. Theor. Appl. Mech. **1**, 859–880 (1982).

[74] George Bugliarello and John W Hayden, "Detailed characteristics of the flow of blood in vitro," Trans. Soc. Rheol. **7**, 209–230 (1963).

[75] AR Pries, TW Secomb, P Gaehtgens, and JF Gross, "Blood flow in microvascular networks. experiments and simulation." Circulation research **67**, 826–834 (1990).

[76] Sangho Kim, Robert L Kong, Aleksander S Popel, Marcos Intaglietta, and Paul C Johnson, "Temporal and spatial variations of cell-free layer width in arterioles," Am. J. Physiol.: Heart Circ. Physiol. **293**, H1526–H1535 (2007).

[77] Kathrin Müller, Dmitry A Fedosov, and Gerhard Gompper, "Margination of micro- and nano-particles in blood flow and its effect on drug delivery," Sci. Rep. **4** (2014).

[78] GW Schmid-Schönbein, Yuan Y Shih, and Shu Chien, "Morphometry of human leukocytes," Blood **56**, 866–875 (1980).

[79] Jean-Michel Paulus, "Platelet size in man," Blood **46**, 321–336 (1975).

[80] GW Schmid-Schönbein, KL Sung, H Tözeren, R Skalak, and S Chien, "Passive mechanical properties of human leukocytes." Biophys. J. **36**, 243 (1981).

[81] Wilbur A Lam, Ovijit Chaudhuri, Ailey Crow, Kevin D Webster, Ashley Kita, James Huang, Daniel A Fletcher, *et al.*, "Mechanics and contraction dynamics of single platelets and implications for clot stiffening," Nat. Mater. **10**, 61–66 (2011).

[82] Denis Semwogerere, Jeffrey F Morris, and Eric R Weeks, "Development of particle migration in pressure-driven flow of a brownian suspension," J. Fluid Mech. **581**, 437–451 (2007).

[83] Marmar Mehrabadi, David N Ku, and Cyrus K Aidun, "Effects of shear rate, confinement, and particle parameters on margination in blood flow," Phys. Rev. E **93**, 023109 (2016).

[84] Timm Krüger, Badr Kaoui, and Jens Harting, "Interplay of inertia and deformability on rheological properties of a suspension of capsules," **751**, 725–745 (2014).